

CONVERGENCE ANALYSIS OF A STOCHASTIC INTERACTING PARTICLE-FIELD ALGORITHM FOR 3D PARABOLIC-PARABOLIC KELLER-SEGEL SYSTEMS*

BOYI HU[†], ZHONGJIAN WANG[‡], JACK XIN[§], AND ZHIWEN ZHANG[¶]

Abstract. Chemotaxis models describe the movement of organisms in response to chemical gradients. In this paper, we present a stochastic interacting particle-field algorithm with a random batch approximation (SIPF- r) for the three-dimensional (3D) parabolic-parabolic Keller-Segel (KS) system, also referred to as the fully parabolic KS system. The SIPF- r method approximates the KS system by coupling particle-based representations of the density with a smooth field variable computed using spectral methods. By incorporating the random batch method (RBM), we bypass the mean-field limit and significantly reduce computational complexity. Under mild assumptions on the regularity of the original KS system and the boundedness of numerical approximations, we prove that the empirical measure of the SIPF- r particle system converges, with high probability, to the exact measure of the limiting McKean-Vlasov process in the 1-Wasserstein distance. Finally, we present numerical experiments to validate the theoretical convergence rates, and demonstrate the performance and robustness of the SIPF- r method as a diagnostic tool for intense focusing and potential finite-time singularity in 3D, subject to critical initial mass thresholds in the system.

Key words. Fully parabolic Keller-Segel system, stochastic interacting particle-field algorithm, random batch, convergence analysis, 3D simulations.

MSC codes. 35K51, 65C05, 65M12, 65M75, 65T50.

1. Introduction. Chemotaxis is a biological phenomenon involving the movement of organisms (e.g., bacteria) in response to signals (e.g., chemo-attractants), which can be produced by the organisms themselves. Theoretical and mathematical modeling of this phenomenon was initiated by Patlak [27], and by Keller and Segel [18]. In this work, we focus on the fully parabolic KS system as follows:

$$(1.1) \quad \begin{aligned} \rho_t &= \nabla \cdot (\mu \nabla \rho - \chi \rho \nabla c), \\ \epsilon c_t &= \Delta c - \lambda^2 c + \rho, \quad \mathbf{x} \in \Omega \subseteq \mathbb{R}^d, \quad t \in [0, T], \end{aligned}$$

where χ, μ are positive constants, and ϵ, λ are non-negative constants. The model is called elliptic if $\epsilon = 0$, and parabolic if $\epsilon > 0$. Here, ρ denotes the density of active particles (bacteria), and c represents the concentration of chemo-attractants emitted by these bacteria. The model finds broad applications in biology, ecology, and medicine [28, 26, 2, 32].

The nonlinear, potentially singular behavior of KS equations, especially blow-up phenomena [25, 14, 1, 9], makes numerical methods essential. Mesh-based methods such as finite difference [4, 31, 7], finite element [29, 8, 30], and finite volume schemes [10, 5, 38] are widely employed. Recent advances include local discontinuous Galerkin methods with optimal convergence rates [20] and semi-discrete symmetrization-based

*Submitted to the editors DATE.

[†]Department of Mathematics, The University of Hong Kong, Pokfulam Road, Hong Kong SAR, P.R.China. huhu22@connect.hku.hk

[‡]Division of Mathematical Sciences, School of Physical and Mathematical Sciences, Nanyang Technological University, 21 Nanyang Link, Singapore 637371. zhongjian.wang@ntu.edu.sg

[§]Corresponding author. Department of Mathematics, University of California at Irvine, Irvine, CA 92697, USA. jack.xin@uci.edu

[¶]Corresponding author. Department of Mathematics, The University of Hong Kong, Pokfulam Road, Hong Kong SAR, P.R.China. Materials Innovation Institute for Life Sciences and Energy (MILES), HKU-SIRI, Shenzhen, P.R. China. zhangzw@hku.hk

schemes that avoid nonlinear solvers [21]. Despite their success, challenges remain in ensuring stability, convergence, and effective handling of singularities, making numerical studies on the KS model an active and evolving field of research.

In addition to mesh-based methods, particle-based approaches have also been developed to address the challenges posed by the KS system, providing a complementary perspective. Stevens [34] developed an N -particle system and established its convergence for the fully parabolic case. Haškovec and Schmeiser [13] proposed a convergent regularized particle system for the 2D parabolic-elliptic KS model. Moreover, Godinho and Quininao [11] showed well-posedness results and the propagation of chaos property in a subcritical KS equation. Craig and Bertozzi [6] proved the convergence of a blob method for the related aggregation equation. Liu and Yang [22] introduced a random particle blob method with a mollified kernel for the parabolic-elliptic case, proving its convergence when the macroscopic mean field equation possesses a global weak solution [23].

In [37], we proposed a novel stochastic interacting particle-field (SIPF) algorithm for the fully parabolic KS system (1.1) in 3D. The SIPF method approximates the KS solution ρ as the empirical measure of particles (see Eq. (2.1)) coupled with a smoother field variable c computed using the spectral method (see Eq. (2.2)). The algorithm employs an implicit Euler discretization and a one-step recursion based on Green's function, which efficiently captures focusing behavior and potentially finite-time blowup with only dozens of Fourier modes in each dimension.

Despite the algorithm's numerical efficiency and stability observed in [37], a complete convergence analysis remains open. This paper fills that gap by establishing and validating convergence estimates for SIPF- r -a random-batch variant designed to reduce the computational cost. Our main result, presented in Theorem 3.2, establishes the convergence of the solution $(\tilde{\rho}, \tilde{c})$ obtained by the SIPF- r method to the exact solution (ρ, c) under mild assumptions. Specifically, the 1-Wasserstein distance between the SIPF- r and exact density distributions, denoted as $\mathcal{W}_1(\tilde{\rho}_t, \rho_t)$, depends on the time step δt , the number H of Fourier modes, and the number of particles P , and scales as $\mathcal{O}(\frac{1}{H^2} + \sqrt{\frac{\delta t}{P}} + \delta t)$. The proof, detailed in Section 3, builds upon key lemmas that quantify single-step update errors and analyze their propagation over time.

The error between the chemical concentration \tilde{c} in the SIPF- r method and the exact solution c originates from Fourier truncation and implicit Euler time discretization. Under appropriate regularity assumptions on c , the truncation error decays as the number of Fourier modes H increases. The temporal error can be expressed through differences between Fourier coefficients of \tilde{c} and c , which further couples with the L^2 particle trajectory error $\mathbb{E}(\|\tilde{X}_t - X_t\|_{L^2})$ accumulated from the preceding step. Here X_t and \tilde{X}_t are the exact dynamics of the system associated with the density and their numerical approximations obtained via our methods, respectively.

At the numerical discretization level, the RBM [17, 16, 15, 3] is incorporated into the SIPF- r method, which renders the particles fully independent and identically distributed (i.i.d.), thereby effectively circumventing the need to address the propagation of chaos [23]. At each time step, small random batches of particles are selected with replacement for particle interactions. In the error estimate between \tilde{c} and c , the i.i.d. property, together with the complex-valued mean value theorem [24] and Bernstein's inequality, bounds deviations of the empirical mean of particle trajectories from its expectation. This deviation accounts for the uncertainty described in Theorem 3.2. Numerical experiments in Section 4 further demonstrate that, with the introduction

of the RBM, the numerical examples maintain a high level of accuracy.

The error between X_t and \tilde{X}_t is influenced by the gradient of c and \tilde{c} , reflecting the dependence of the particle trajectories on the interaction potential. Using Parseval's identity [19], we relate $\|\nabla\tilde{c} - \nabla c\|_{L^2}$ to Fourier-coefficient errors, establishing two coupled recursive inequalities between $\|\nabla\tilde{c} - \nabla c\|_{L^2}$ and $\mathbb{E}(\|\tilde{X}_t - X_t\|_{L^2})$. The first inequality relates $\|\nabla\tilde{c} - \nabla c\|_{L^2}$ to $\mathbb{E}(\|\tilde{X}_t - X_t\|_{L^2})$; the second updates $\mathbb{E}(\|\tilde{X}_t - X_t\|_{L^2})$ by incorporating a $\|\nabla\tilde{c} - \nabla c\|_{L^2}$ term (see Eqs. (3.58)-(3.59)). Substituting and decoupling these aforementioned recursive inequalities yields a bound for $\mathbb{E}(\|\tilde{X}_t - X_t\|_{L^2})$ that depends only on earlier errors. Through the natural coupling $\gamma_t = \text{Law}(\tilde{X}_t, X_t)$, this L^2 error estimate translates to the 1-Wasserstein distance $\mathcal{W}_1(\tilde{\rho}_t, \rho_t)$. Applying the discrete Gronwall inequality together with Fourier-coefficient error estimates leads to the global convergence result in Theorem 3.2.

In addition to the theoretical analysis, Section 4 provides comprehensive numerical experiments to validate the performance of the SIPF- r method. These experiments verify the predicted convergence rates, confirm the validity of the regularity assumptions, and explore the complex dynamics of the KS system. A particular focus is placed on the analytically elusive 3D critical mass threshold. In Subsection 4.2, the SIPF- r algorithm identifies blow-up regimes and captures intense focusing towards finite-time singularities (see Figures 4 and 6). Notably, the method remains robust in detecting blow-up even under practical discretization parameters $(H, P, \delta t)$ that are significantly more relaxed than the stringent constraints required for the convergence proof (illustrated in Figure 5).

The rest of the paper is organized as follows. In Section 2, we review the SIPF method for solving the fully parabolic KS system and present the derivation of the SIPF- r method, which incorporates the RBM to compute the particle interaction. In Section 3, under certain assumptions, we provide a detailed convergence analysis of the SIPF- r method, which decomposes the proof into several lemmas. In Section 4, we present numerical results to validate the necessity of the assumptions, demonstrate the accuracy of the SIPF- r method, and confirm the theoretical convergence rate derived in our analysis. Finally, the paper is concluded in Section 5.

2. Derivation of the SIPF- r Method. In this section, we present the SIPF- r method for solving the fully parabolic KS model. Since the evolutionary phenomena of interest occur in the interior of the domain, we restrict the system (1.1) to a large domain $\Omega = [-L/2, L/2]^3$ and assume the Dirichlet boundary condition for particle density ρ and the Neumann boundary condition for chemical concentration c .

Throughout this section, we use the standard notation ρ, c , etc., to represent the exact solutions of the fully parabolic KS model. For the variables computed or approximated using the SIPF- r algorithm, we instead use the notations $\tilde{\rho}, \tilde{c}$, etc.

As a numerical algorithm, we assume that the temporal domain $[0, T]$ is partitioned by $\{t_n\}_{n=0:n_T}$ with $t_0 = 0$ and $t_{n_T} = T$. We approximate the density $\tilde{\rho}$ at $t = t_n$ by empirical particles $\{\tilde{X}_{t_n}^p\}_{p=1:P}$, i.e.,

$$(2.1) \quad \tilde{\rho}_{t_n} \approx \frac{M_0}{P} \sum_{p=1}^P \delta(x - \tilde{X}_{t_n}^p), \quad P \gg 1,$$

where M_0 denotes the conserved total mass (integral of ρ over the domain Ω). For the chemical concentration \tilde{c} , we adopt a Fourier basis approximation, namely, $\tilde{c}(\mathbf{x}, t)$

has a series representation

$$(2.2) \quad \tilde{c}(\mathbf{x}, t) = \sum_{\mathbf{j} \in \mathcal{H}} \tilde{\alpha}_{t;\mathbf{j}} \exp(i2\pi j_1 x_1/L) \exp(i2\pi j_2 x_2/L) \exp(i2\pi j_3 x_3/L),$$

where \mathcal{H} denotes the index set

$$(2.3) \quad \mathcal{H} = \{\mathbf{j} \in \mathbb{N}^3 : |j_1|, |j_2|, |j_3| \leq \frac{H}{2}\},$$

and $i = \sqrt{-1}$. The exact solution $c(\mathbf{x}, t)$ can also be approximated by a truncated spatial Fourier series expansion as follows:

$$(2.4) \quad c(\mathbf{x}, t) \approx \sum_{\mathbf{j} \in \mathcal{H}} \alpha_{t;\mathbf{j}} \exp(i2\pi j_1 x_1/L) \exp(i2\pi j_2 x_2/L) \exp(i2\pi j_3 x_3/L).$$

Remark 2.1. The choice of the Fourier basis over Hermite polynomials for approximating the chemical concentration is based on the fact that, since the blow-up phenomenon is localized in the domain interior, periodic boundary conditions effectively emulate an infinite spatial domain under this configuration. When the spatial localization of the singularity remains distant from domain boundaries, its interaction with these artificial edges becomes negligible.

Then at $t_0 = 0$, we generate P empirical samples $\{\tilde{X}_0^p\}_{p=1:P}$ according to the initial condition of $\tilde{\rho}_0$ and set up $\tilde{\alpha}_{0;\mathbf{j}}$ using the Fourier series of \tilde{c}_0 . For ease of presenting our algorithm, with a slight abuse of notation, we use $\tilde{\rho}_n = \frac{M_0}{P} \sum_{p=1}^P \delta(x - \tilde{X}_n^p)$, and

$$(2.5) \quad \tilde{c}_n = \sum_{\mathbf{j} \in \mathcal{H}} \tilde{\alpha}_{n;\mathbf{j}} \exp(i2\pi j_1 x_1/L) \exp(i2\pi j_2 x_2/L) \exp(i2\pi j_3 x_3/L)$$

to represent density $\tilde{\rho}$ and chemical concentration \tilde{c} at time t_n .

Considering the time-stepping for the system (1.1) from t_n to t_{n+1} , with $\tilde{\rho}_n$ and \tilde{c}_{n-1} known, our algorithm, inspired by the operator splitting technique, consists of two sub-steps: updating chemical concentration \tilde{c} and updating organism density $\tilde{\rho}$.

Updating chemical concentration \tilde{c} . Let $\delta t = t_{n+1} - t_n > 0$ be the time step. We discretize the \tilde{c} equation of (1.1) in time by an implicit Euler scheme

$$(2.6) \quad \epsilon(\tilde{c}_n - \tilde{c}_{n-1})/\delta t = (\Delta - \lambda^2)\tilde{c}_n + \tilde{\rho}_n.$$

From Eq. (2.6), we obtain the explicit formula for \tilde{c}_n as follows:

$$(2.7) \quad (\Delta - \lambda^2 - \epsilon/\delta t)\tilde{c}_n = -\epsilon\tilde{c}_{n-1}/\delta t - \tilde{\rho}_n.$$

It follows that

$$(2.8) \quad \tilde{c}_n = \tilde{c}(\mathbf{x}, t_n) = -\mathcal{K}_{\epsilon, \delta t} * (\epsilon\tilde{c}_{n-1}/\delta t + \tilde{\rho}_n) = -\mathcal{K}_{\epsilon, \delta t} * (\epsilon\tilde{c}(\mathbf{x}, t_{n-1})/\delta t + \tilde{\rho}(\mathbf{x}, t_n)),$$

where $\mathcal{K}_{\epsilon, \delta t}$ is the Green's function of the operator $\Delta - \lambda^2 - \epsilon/\delta t$ and $*$ represents an approximation of spatial convolution, which is not the same as in the continuous setup, as \tilde{c} is computed using truncated Fourier basis functions and $\tilde{\rho}$ is given by a

discrete particle representation. Unless otherwise stated, all subsequent norms $\|\cdot\|$ will refer to the L^2 norms. In case of \mathbb{R}^3 , the Green's function $\mathcal{K}_{\epsilon,\delta t}$ reads as follows:

$$(2.9) \quad \mathcal{K}_{\epsilon,\delta t} = \mathcal{K}_{\epsilon,\delta t}(\mathbf{x}) = -\frac{\exp\{-\beta\|\mathbf{x}\|\}}{4\pi\|\mathbf{x}\|}, \quad \beta = \sqrt{\lambda^2 + \epsilon/\delta t}.$$

Green's function admits a closed-form Fourier transform,

$$(2.10) \quad \mathcal{F}\mathcal{K}_{\epsilon,\delta t}(\omega) = -\frac{1}{\|\omega\|^2 + \beta^2}.$$

For the term $-\mathcal{K}_{\epsilon,\delta t} * \tilde{c}_{n-1}$ in Eq. (2.8), by Eq. (2.10) it is equivalent to modify Fourier coefficients $\tilde{\alpha}_{\mathbf{j}}$ to $\tilde{\alpha}_{\mathbf{j}}/(4\pi^2 j_1^2/L^2 + 4\pi^2 j_2^2/L^2 + 4\pi^2 j_3^2/L^2 + \beta^2)$.

For the second term $\mathcal{K}_{\epsilon,\delta t} * \tilde{\rho}$, we first approximate $\mathcal{K}_{\epsilon,\delta t}$ with a cosine series expansion, then according to the particle representation of $\tilde{\rho}$ in Eq. (2.1),

$$(2.11) \quad (\mathcal{K}_{\epsilon,\delta t} * \tilde{\rho})_{\mathbf{j}} \approx \frac{M_0}{P} \sum_{p=1}^P \frac{\exp(-i2\pi j_1 \tilde{X}_{n,1}^p/L - i2\pi j_2 \tilde{X}_{n,2}^p/L - i2\pi j_3 \tilde{X}_{n,3}^p/L) (-1)^{j_1+j_2+j_3}}{4\pi^2 j_1^2/L^2 + 4\pi^2 j_2^2/L^2 + 4\pi^2 j_3^2/L^2 + \beta^2}.$$

Finally, we summarize the one-step update of the Fourier coefficients of the chemical concentration \tilde{c} in Algorithm 2.1, which follows the same procedure as in the original SIPF method [37].

Algorithm 2.1 One-step update of chemical concentration in the SIPF- r method

Require: Distribution $\tilde{\rho}_n$ represented by empirical samples \tilde{X}_n , initial concentration \tilde{c}_{n-1} represented by Fourier coefficients $\tilde{\alpha}_{n-1}$.

- 1: **for** $\mathbf{j} \in \mathcal{H}$ **do**
- 2: $\tilde{\alpha}_{n;\mathbf{j}} \leftarrow \frac{\epsilon \tilde{\alpha}_{n-1;\mathbf{j}}}{\delta t(4\pi^2 j_1^2/L^2 + 4\pi^2 j_2^2/L^2 + 4\pi^2 j_3^2/L^2 + \beta^2)}$
- 3: $F_{\mathbf{j}} \leftarrow 0$
- 4: **for** $p = 1$ **to** P **do**
- 5: $F_{\mathbf{j}} \leftarrow F_{\mathbf{j}} + \exp(-i2\pi j_1 \tilde{X}_{n,1}^p/L - i2\pi j_2 \tilde{X}_{n,2}^p/L - i2\pi j_3 \tilde{X}_{n,3}^p/L)$
- 6: **end for**
- 7: $F_{\mathbf{j}} \leftarrow F_{\mathbf{j}} \cdot \frac{(-1)^{j_1+j_2+j_3}}{4\pi^2 j_1^2/L^2 + 4\pi^2 j_2^2/L^2 + 4\pi^2 j_3^2/L^2 + \beta^2} \cdot \frac{M_0}{P}$
- 8: **end for**
- 9: $\tilde{\alpha}_n \leftarrow \tilde{\alpha}_n - F$

Ensure: Updated chemical concentration field from \tilde{c}_{n-1} to \tilde{c}_n via $\tilde{\alpha}_n$.

Updating density of active particles $\tilde{\rho}$. In the one-step update of density $\tilde{\rho}_n$ represented by particles $\{\tilde{X}_n^p\}_{p=1:P}$, we apply Euler-Maruyama scheme to solve the SDE

$$(2.12) \quad \tilde{X}_{n+1}^p = \tilde{X}_n^p + \chi \nabla_{\mathbf{x}} \tilde{c}(\tilde{X}_n^p, t_n) \delta t + \sqrt{2\mu \delta t} N_n^p,$$

where N_n^p 's are i.i.d. standard normal random variables corresponding to the Brownian paths in the SDE formulation. For $n > 1$, substituting Eq. (2.8) in Eq. (2.12) gives:

$$(2.13) \quad \tilde{X}_{n+1}^p = \tilde{X}_n^p - \chi \nabla_{\mathbf{x}} \mathcal{K}_{\epsilon,\delta t} * (\epsilon \tilde{c}_{n-1}(\mathbf{x})/\delta t + \tilde{\rho}_n(\mathbf{x}))|_{\mathbf{x}=\tilde{X}_n^p} \delta t + \sqrt{2\mu \delta t} N_n^p,$$

from which $\tilde{\rho}_{n+1}(\mathbf{x})$ is constructed via Eq. (2.1).

In this particle formulation, the computation of the spatial convolution differs slightly from that in the update of \tilde{c} (i.e., Eq. (2.8)).

For the term $\nabla_{\mathbf{x}}\mathcal{K}_{\epsilon,\delta t} * \tilde{c}_{n-1}(\tilde{X}_n^p)$, to avoid the singular points of $\nabla_{\mathbf{x}}\mathcal{K}_{\epsilon,\delta t}$, we evaluate the integral with quadrature points that are away from 0. Precisely, denote the standard quadrature point in Ω as

$$(2.14) \quad x_{\mathbf{j}} = (j_1 L/H, j_2 L/H, j_3 L/H),$$

where j_1, j_2, j_3 are integers ranging from $-H/2$ to $H/2 - 1$. When computing $\nabla_{\mathbf{x}}\mathcal{K}_{\epsilon,\delta t} * \tilde{c}_{n-1}(\tilde{X}_n^p)$, we evaluate $\nabla_{\mathbf{x}}\mathcal{K}_{\epsilon,\delta t}$ at $\{\tilde{X}_n^p + \bar{X}_n^p - x_{\mathbf{j}}\}_{\mathbf{j}}$, where a small spatial shift is defined as $\bar{X}_n^p = \frac{L}{2H} + \lfloor \frac{\tilde{X}_n^p}{L/H} \rfloor \frac{L}{H} - \tilde{X}_n^p$ and \tilde{c} at $\{x_{\mathbf{j}} - \bar{X}_n^p\}_{\mathbf{j}}$ correspondingly. The latter is computed by inverse Fourier transform of the shifted coefficients, with $\tilde{\alpha}_{\mathbf{j}}$ modified to $\tilde{\alpha}_{\mathbf{j}} \exp(-i2\pi j_1 \bar{X}_{n;1}^p/L - i2\pi j_2 \bar{X}_{n;2}^p/L - i2\pi j_3 \bar{X}_{n;3}^p/L)$, where $(\bar{X}_{n;i}^p)$ denotes the i -th component of \bar{X}_n^p .

Motivated by mini-batch sampling [12, 33, 35, 36] and the random batch method (RBM) [17, 16, 3, 15], for each particle \tilde{X}_n^p , we choose a small batch C_p of size R randomly with replacement. We restrict the interaction of \tilde{X}_n^p to particles within this batch; specifically, we approximate the interaction term $\chi\delta t \nabla_{\mathbf{x}}\mathcal{K}_{\epsilon,\delta t} * \tilde{\rho}(\tilde{X}_n^p, t_n)$ by the random batch sum $\sum_{s \in C_p, s \neq p} \frac{\chi M_0 \delta t}{R} \nabla_{\mathbf{x}}\mathcal{K}_{\epsilon,\delta t}(\tilde{X}_n^p - \tilde{X}_n^s)$.

We summarize the one-step update (for $n > 1$) of the density in the SIPF- r method as in Algorithm 2.2.

Algorithm 2.2 One-step update of density in the SIPF- r method

Require: Distribution $\tilde{\rho}_n$ represented by empirical samples \tilde{X}_n , concentration \tilde{c}_{n-1} represented by Fourier coefficients $\tilde{\alpha}_{n-1}$.

- 1: **for** $p = 1$ **to** P **do**
- 2: $\tilde{X}_{n+1}^p \leftarrow \tilde{X}_{n+1}^p + \sqrt{2\mu\delta t} N_n^p$ { N_n^p is a standard normal random variable}
- 3: $C_p \leftarrow$ random subset of $\{1, \dots, P\}$ with replacement, size R
- 4: $\tilde{X}_{n+1}^p \leftarrow \tilde{X}_{n+1}^p - \sum_{s \in C_p} \frac{\chi M_0 \delta t}{R} \nabla_{\mathbf{x}}\mathcal{K}_{\epsilon,\delta t}(\tilde{X}_n^p - \tilde{X}_n^s)$
- 5: $\bar{X}_n^p \leftarrow \frac{L}{2H} + \lfloor \frac{\tilde{X}_n^p}{L/H} \rfloor \frac{L}{H} - \tilde{X}_n^p$
- 6: **for** $(\mathbf{j}) \in \mathcal{H}$ **do**
- 7: $F_{\mathbf{j}} \leftarrow \nabla_{\mathbf{x}}\mathcal{K}_{\epsilon,\delta t}(\tilde{X}_n^p + \bar{X}_n^p - x_{\mathbf{j}})$ { $x_{\mathbf{j}}$ from Eq. (2.14)}
- 8: $G_{\mathbf{j}} \leftarrow \tilde{\alpha}_{\mathbf{j}} \exp(-i2\pi j_1 \bar{X}_{n;1}^p/L - i2\pi j_2 \bar{X}_{n;2}^p/L - i2\pi j_3 \bar{X}_{n;3}^p/L)$
- 9: **end for**
- 10: $\check{G} \leftarrow \text{iFFT}(G)$
- 11: $\tilde{X}_{n+1}^p \leftarrow \tilde{X}_{n+1}^p - \epsilon \chi(F, \check{G}) \frac{L^3}{H^3}$ { $(\cdot, \cdot) \frac{L^3}{H^3}$ denotes an inner product corresponding to $L^2(\Omega)$ quadrature}
- 12: **end for**

Ensure: Updated distribution $\tilde{\rho}_{n+1}$ represented by \tilde{X}_{n+1} .

Combining Eq. (2.8) and Eq. (2.13), we conclude that the recursion from $(\{\tilde{X}_n^p\}_{p=1:P}, \tilde{\rho}_n(\mathbf{x}), \tilde{c}_{n-1}(\mathbf{x}))$ to $(\{\tilde{X}_{n+1}^p\}_{p=1:P}, \tilde{\rho}_{n+1}(\mathbf{x}), \tilde{c}_n(\mathbf{x}))$ is thus fully defined. We summarize the SIPF- r method in the following Algorithm 2.3.

Computational Complexity. We briefly analyze the complexity of the proposed SIPF- r method. The memory usage is $\mathcal{O}(P + |\mathcal{H}|)$, where $|\mathcal{H}|$ denotes the total number of Fourier modes. Regarding the computational cost, the original SIPF method

Algorithm 2.3 Stochastic Interacting Particle-Field Method

Require: Initial distribution ρ_0 , initial concentration c_0 .

1: Generate P i.i.d. samples according to distribution ρ_0 : $X_0^1, X_0^2, \dots, X_0^P$.

2: **for** $p = 1$ **to** P **do**

3: Compute \tilde{X}_1^p by Eq. (2.12), with $c_{-1} = c_0$.

4: **end for**

5: Compute \tilde{c}_1 by Alg. 2.1 with c_0 and $\tilde{\rho}_1 = \sum_{p=1}^P \frac{M_0}{P} \delta_{\tilde{X}_1^p}$.

6: **for** $n = 2$ **to** $N = \lfloor T/\delta t \rfloor$ **do**

7: Compute \tilde{X}_n by Alg. 2.2 with $\tilde{\rho}_{n-1}$ and \tilde{c}_{n-2} .

8: Compute \tilde{c}_n by Alg. 2.1 with \tilde{c}_{n-1} and $\tilde{\rho}_n = \sum_{p=1}^P \frac{M_0}{P} \delta_{\tilde{X}_n^p}$.

9: **end for**

Ensure: Final particle distribution $\tilde{\rho}_N$ and concentration field \tilde{c}_N .

typically requires $\mathcal{O}(P^2)$ operations for pairwise particle interactions. In contrast, by incorporating the RBM, the interaction cost in the SIPF- r method is reduced to $\mathcal{O}(PR)$, where R is the batch size.

The overall per-step complexity of Algorithm 2.3 is $\mathcal{O}(PR + P|\mathcal{H}| \log(|\mathcal{H}|))$. Crucially, the error analysis in Theorem 3.2 reveals that the error introduced by the random batch approximation scales only as $\mathcal{O}(\delta t/\sqrt{R})$. This allows us to choose $R \ll P$ (e.g., $R = 100$ vs. $P = 10^4$) to achieve a substantial speedup while maintaining the desired accuracy.

Particle-wise Independence due to RBM. In the above derivation, $\{\tilde{X}_n^p\}_{p=1:P}$ are i.i.d. samples with distribution $\tilde{\rho}_n$ and independent of \tilde{c}_{n-1} . The one-step trajectories follow the discrete-time rule:

$$(2.15) \quad \tilde{X}_{t_{n+1}} = \tilde{X}_{t_n} + \chi \nabla \tilde{c}(\tilde{X}_{t_n}, t_n) \delta t + \int_{t_n}^{t_{n+1}} \sqrt{2\mu} dW_s,$$

where $\nabla \tilde{c}$ is computed via Eq. (2.8), and W_s denotes the Brownian motion. It is worth noting that, for the updated position of the p -th particle \tilde{X}_{n+1}^p by Eq. (2.12), the interaction term, $\nabla_{\mathbf{x}} \mathcal{K}_{\epsilon, \delta t} * \tilde{\rho}(\tilde{X}_n^p, t_n)$ is computed by $\sum_{s \in C_p, s \neq p} \frac{\chi M_0 \delta t}{R} \nabla_{\mathbf{x}} \mathcal{K}_{\epsilon, \delta t}(\tilde{X}_n^p - \tilde{X}_n^s)$, where the selection of C_p is independent of \tilde{X}_n^p and hence $\{\tilde{X}_n^s\}_{s \in C_p}$ can be viewed as i.i.d. samples of $\tilde{\rho}_n$ independent of \tilde{c}_{n-1} and \tilde{X}_n^p . Together with the independent Brownian motion term, we can deduce the independence of $\{\tilde{X}_{n+1}^p\}_{p=1:P}$.

Correspondingly, we denote the exact dynamics of the system by X_t , a $\rho(\cdot, t)$ -distributed random variable evolving continuously in time:

$$(2.16) \quad X_t = X_{t_0} + \chi \int_{t_0}^t \nabla c(X_s, s) ds + \int_{t_0}^t \sqrt{2\mu} dW_s, \quad X_{t_0} = \tilde{X}_{t_0},$$

where $c(\cdot, s)$ is the exact concentration field, and the integral describes how the gradient field evolves in continuous time. Both processes share the same Brownian motion W_s , indicating that both processes are driven by the same source of randomness.

3. L^2 Convergence of the SIPF- r method to smooth solutions. We now prove the convergence of the SIPF- r method to classical solutions of the 3D parabolic-parabolic Keller-Segel equations. To ensure the validity of the following analysis, we introduce a set of assumptions that impose structure on the concentration fields and their gradients.

3.1. Assumptions and Theorem Statement. To establish the convergence analysis of the SIPF- r method, we first introduce assumptions that ensure the boundedness of approximation errors for particles and gradients of the chemical concentration at any finite time t . Specifically, we make the following assumptions.

ASSUMPTION 1. *There exist constants $M_1, M_2 > 0$ such that for all $t \in [0, T]$ and $\mathbf{x} \in \mathbb{R}^3$,*

$$(3.1) \quad \|\tilde{X}_t - X_t\| \leq M_1,$$

$$(3.2) \quad \|\nabla\tilde{c}(\mathbf{x}, t) - \nabla c(\mathbf{x}, t)\| \leq M_2.$$

We note that this assumption only requires the errors to be bounded, but does not require them to converge to zero. The convergence of these errors to zero will be established in the subsequent theorems. Furthermore, the boundedness condition in Eq. (3.1) can be derived from Eqs. (2.15)-(2.16) and Assumption 2(c); Eq. (3.2) follows directly from the uniform bound in Assumption 2(c) detailed later.

ASSUMPTION 2. *Suppose both $\nabla\tilde{c}$ and ∇c satisfy Lipschitz continuity conditions in space and time, along with regularity and boundedness properties as follows:*

(a) (Spatial Lipschitz Continuity) *There exists a constant $K > 0$, depending on the regularity of $\nabla\tilde{c}$ and ∇c , as well as the parameters ϵ and λ in the system (1.1), such that for all $t \in [0, T]$ and $\mathbf{x}, \mathbf{y} \in \mathbb{R}^3$,*

$$(3.3) \quad \max(\|\nabla\tilde{c}(\mathbf{x}, t) - \nabla\tilde{c}(\mathbf{y}, t)\|, \|\nabla c(\mathbf{x}, t) - \nabla c(\mathbf{y}, t)\|) \leq K\|\mathbf{x} - \mathbf{y}\|.$$

This implies that the second derivatives (Hessian entries) $\nabla^2\tilde{c}(\mathbf{x}, t)$ exist almost everywhere and satisfy:

$$(3.4) \quad \sup_{\mathbf{x} \in \mathbb{R}^3, t \in [0, T]} (\|\nabla^2\tilde{c}(\mathbf{x}, t)\|) \leq K.$$

(b) (Temporal Lipschitz Continuity) *There exists a constant $K_1 > 0$, depending on the regularity of ∇c and the parameters ϵ and λ in the system (1.1), such that for any $t_1, t_2 \in [0, T]$ and $\mathbf{x} \in \mathbb{R}^3$,*

$$(3.5) \quad \|\nabla c(\mathbf{x}, t_1) - \nabla c(\mathbf{x}, t_2)\| \leq K_1|t_1 - t_2|.$$

(c) (Uniform Boundedness) *There exists a constant $M_3 > 0$, depending on the regularity of ∇c and the parameters ϵ and λ in the system (1.1), such that for all $t \in [0, T]$ and $\mathbf{x} \in \mathbb{R}^3$:*

$$(3.6) \quad \max(\|\nabla c(\mathbf{x}, t)\|, \|\nabla\tilde{c}(\mathbf{x}, t)\|) \leq M_3.$$

(d) (Regularity of Time Derivatives) *The exact solution $c(\mathbf{x}, t)$ is assumed to be sufficiently smooth in time and space such that both $\partial_t^2 c(\mathbf{x}, t)$ and $\nabla\partial_t^2 c(\mathbf{x}, t)$ are bounded. There exists a constant $K_2 > 0$ such that for all $t \in [0, T]$:*

$$(3.7) \quad \max\left(\sup_{\mathbf{x} \in \mathbb{R}^3} \|\partial_t^2 c(\mathbf{x}, t)\|, \sup_{\mathbf{x} \in \mathbb{R}^3} \|\nabla\partial_t^2 c(\mathbf{x}, t)\|\right) \leq K_2.$$

Remark 3.1. These regularity and boundedness conditions reflect inherent properties of the SIPF- r method rather than external constraints on the KS system. As analyzed in Subsection 3.4, the discrete Fourier representation and Brownian diffusion naturally impose spectral regularity and suppress singular clustering, ensuring $\nabla\tilde{c}$ remains well-behaved throughout the computation. The boundedness conditions in Assumption 2 are validated through numerical simulations in Subsection 4.1.1.

We now state our main theorem, which quantifies the convergence of the SIPF- r method.

THEOREM 3.2. *Suppose that the exact solutions and the numerical solutions of the SIPF- r method satisfy Assumptions 1 and 2 in \mathbb{R}^3 . Let H denote the number of Fourier modes, P denote the number of particles, R denote the batch size, and δt denote the uniform time step in the SIPF- r method, respectively. Then the quantities $(\tilde{\rho}, \tilde{c})$, which are the numerical solutions of the SIPF- r method, exist on discrete time steps $t_n = n\delta t$ for $n = 0, 1, \dots, \lfloor T/\delta t \rfloor$, and satisfy the following error estimates with high probability:*

For all $n \in \{0, 1, \dots, \lfloor T/\delta t \rfloor\}$, the 1-Wasserstein distance (defined in Eq. (3.64)) between $\tilde{\rho}_{t_n}$ and ρ_{t_n} satisfies $\mathcal{W}_1(\tilde{\rho}_{t_n}, \rho_{t_n})$ is $\mathcal{O}\left(\frac{1}{H^2} + \sqrt{\frac{\delta t}{P}} + \delta t\right)$, and the maximum error in the truncated Fourier coefficients of \tilde{c}_{t_n} and c_{t_n} satisfies $\max_{j \in \mathcal{H}} \|\tilde{\alpha}_{t_n; j} - \alpha_{t_n; j}\|$ is $\mathcal{O}\left(\frac{1}{H} + \frac{H^2 \delta t}{\sqrt{P}} + H\delta t + \frac{H}{\sqrt{P}}\right)$. More specifically, for all $n \in \{0, 1, \dots, \lfloor T/\delta t \rfloor\}$, the errors are bounded with high probability by:

$$(3.8) \quad \mathcal{W}_1(\tilde{\rho}_{t_n}, \rho_{t_n}) \leq \left(\frac{S_0}{H^2} + S_1 \delta t + S_2 \sqrt{\frac{\delta t}{P}} + \frac{S_3 \delta t}{\sqrt{R}} \right) \cdot \exp(1 + S_4 \sqrt{\delta t}),$$

$$\max_{j \in \mathcal{H}} \|\tilde{\alpha}_{t_n; j} - \alpha_{t_n; j}\| \leq \left(\frac{S_5}{H} + S_6 H \delta t + \frac{S_7 H^2 \delta t}{\sqrt{P}} + \frac{S_8 H \delta t}{\sqrt{R}} \right) \cdot \exp(1 + S_4 \sqrt{\delta t}) + \frac{S_9 H}{\sqrt{P}},$$

where S_i , $i = 0, \dots, 9$, are positive constants specified in Eqs. (3.65)(3.68).

A direct consequence of Theorem 3.2 is that the SIPF- r solution converges to the exact solution as $\delta t \rightarrow 0$ and $H, P \rightarrow \infty$. Specifically, the density $\tilde{\rho}_{t_n}$ converges in the 1-Wasserstein metric even without imposing specific scaling relations between the discretization parameters, as all error terms in the first inequality of Eq. (3.8) naturally vanish. The convergence of the chemical concentration \tilde{c}_{t_n} requires the scaling conditions $H/\sqrt{P} \rightarrow 0$ and $H\delta t \rightarrow 0$ to control the statistical and discretization errors, respectively.

Remark 3.3 (Practical convergence and scaling). The error estimate in Theorem 3.2 explicitly retains the dependence on R to validate the theoretical $\mathcal{O}(1/\sqrt{R})$ convergence rate as verified in Subsection 4.1.2. However, as shown in Eq. (3.8), this stochastic term scales as $\mathcal{O}(\delta t/\sqrt{R})$, rendering it mathematically subordinate to the leading-order discretization errors. Consequently, a fixed moderate batch size (e.g., $R = 100$) suffices in practice, as the total error remains dominated by H and δt rather than the random batch approximation.

Theorem 3.2 also indicates that the error bound for the concentration gradient scales with H in the numerator due to the amplification of high-frequency modes in the process of differentiation. In contrast, the particle density error does not suffer from this amplification, as the particle trajectories result from the time integration of the velocity field, which acts as a low-pass filter, smoothing out the oscillatory gradient noise. In practice, for the 3D KS system, the method performs well with much milder parameter requirements than the worst-case analysis suggests. Numerical experiments in Section 4 show that moderate parameters ($H = 24$, $P = 10^4$, $\delta t = 10^{-4}$) suffice for both convergence validation (Subsection 4.1) and blow-up detection (Subsection 4.2), demonstrating computational feasibility for resolving physically relevant phenomena without prohibitive computational costs.

3.2. Several lemmas. The result of Theorem 3.2 relies on the following lemmas concerning the change in single-step update error of the SIPF- r method. We first prove several lemmas in this subsection and leave the complete proof of Theorem 3.2 to the next subsection.

From Eqs. (2.2)-(2.4), the error between \tilde{c} and c can be decomposed into two components: the error in their Fourier coefficients and the truncation error of c . As the Fourier mode H tends to infinity, and given the smoothness of c , the truncation error becomes negligible and can be omitted from the analysis. We now focus on the error analysis between the Fourier coefficients $\tilde{\alpha}_{\mathbf{j}}$ and $\alpha_{\mathbf{j}}$ of \tilde{c} and c , as presented in the following lemma.

LEMMA 3.4. *For all $n \in \mathbb{N}_+$ and all $\mathbf{j} \in \mathcal{H}$ (the same index set as in Eq. (2.3)), under Assumptions 1 and 2, the following inequality holds with high probability:*

$$\|\tilde{\alpha}_{t_n;\mathbf{j}} - \alpha_{t_n;\mathbf{j}}\| \leq \|\tilde{\alpha}_{t_{n-1};\mathbf{j}} - \alpha_{t_{n-1};\mathbf{j}}\| + C_1 \delta t^2 + \frac{C_2 \|\omega_{\mathbf{j}}\| \delta t}{\sqrt{P}} + C_3 \|\omega_{\mathbf{j}}\| \delta t \mathbb{E}[\|\tilde{X}_{t_n} - X_{t_n}\|],$$

where C_1, C_2, C_3 are constants, and $t_n = n\delta t$.

Proof. We first write the frequency $\omega_{\mathbf{j}} = (\frac{2\pi j_1}{L}, \frac{2\pi j_2}{L}, \frac{2\pi j_3}{L})$, and define the notation $Z_{\mathbf{j}} = (\|\omega_{\mathbf{j}}\|^2 + \lambda^2) \cdot \frac{\delta t}{\epsilon}$, which satisfies $Z_{\mathbf{j}} \rightarrow 0$ as $\delta t \rightarrow 0$. Recall the update formula for the numerical approximation of the Fourier coefficients $\tilde{\alpha}_{t_n;\mathbf{j}}$ (from Eq. (2.8)):

$$(3.9) \quad (1 + Z_{\mathbf{j}})\tilde{\alpha}_{t_n;\mathbf{j}} = \tilde{\alpha}_{t_{n-1};\mathbf{j}} + \frac{\delta t}{\epsilon} \mathcal{F}_{\mathbf{j}}[\tilde{\rho}(\mathbf{x}, t_n)],$$

where $\mathcal{F}_{\mathbf{j}}[\tilde{\rho}(\mathbf{x}, t_n)] = \frac{M_0}{P} \sum_{p=1}^P \frac{e^{-i\omega_{\mathbf{j}} \cdot \tilde{\mathbf{x}}_{t_n}^p}}{1 + Z_{\mathbf{j}}}$ represents the Fourier coefficient of $\tilde{\rho}(\mathbf{x}, t_n)$ at the frequency $\omega_{\mathbf{j}}$.

The exact solution $c(\mathbf{x}, t)$ satisfies the continuous equation:

$$(3.10) \quad \epsilon \frac{\partial c}{\partial t} = \Delta c - \lambda^2 c + \rho.$$

Integrating this equation from t_{n-1} to t_n and applying the Taylor expansion with integral remainder to the time derivative term, such that $c(t_{n-1}) = c(t_n) - \delta t \partial_t c(t_n) + \int_{t_{n-1}}^{t_n} (s - t_{n-1}) \partial_t^2 c(s) ds$, we can express the exact solution in a form compatible with the implicit Euler scheme:

$$(3.11) \quad \frac{c(t_n) - c(t_{n-1})}{\delta t} = \frac{1}{\epsilon} (\Delta c(t_n) - \lambda^2 c(t_n) + \rho(t_n)) + R_n(\mathbf{x}).$$

By Assumption 2(d), $\|\partial_t^2 c\|$ is bounded by K_2 . The temporal truncation error $R_n(\mathbf{x})$ satisfies

$$(3.12) \quad \|R_n\| \leq \frac{\delta t}{2} \sup_{s \in [t_{n-1}, t_n]} \|\partial_t^2 c(\cdot, s)\| \leq C_1 \delta t,$$

where $C_1 = \frac{K_2}{2}$ is a constant. Taking the Fourier transform of the discrete relation for the exact solution and rearranging terms, we get

$$(3.13) \quad (1 + Z_{\mathbf{j}})\alpha_{t_n;\mathbf{j}} = \alpha_{t_{n-1};\mathbf{j}} + \frac{\delta t}{\epsilon} \mathcal{F}_{\mathbf{j}}[\rho(t_n)] + \delta t \mathcal{F}_{\mathbf{j}}[R_n].$$

Combining Eq. (3.13) and Eq. (3.9), we obtain

$$(3.14) \quad \begin{aligned} \|\alpha_{t_n;\mathbf{j}} - \tilde{\alpha}_{t_n;\mathbf{j}}\| &= \frac{1}{1 + Z_{\mathbf{j}}} \left\| (\alpha_{t_{n-1};\mathbf{j}} - \tilde{\alpha}_{t_{n-1};\mathbf{j}}) + \frac{\delta t}{\epsilon} (\mathcal{F}_{\mathbf{j}}[\rho(t_n)] - \mathcal{F}_{\mathbf{j}}[\tilde{\rho}_n]) + \delta t \mathcal{F}_{\mathbf{j}}[R_n] \right\| \\ &\leq \|\alpha_{t_{n-1};\mathbf{j}} - \tilde{\alpha}_{t_{n-1};\mathbf{j}}\| + \frac{\delta t}{\epsilon} \|\mathcal{F}_{\mathbf{j}}[\rho(t_n)] - \mathcal{F}_{\mathbf{j}}[\tilde{\rho}_n]\| + \delta t \|\mathcal{F}_{\mathbf{j}}[R_n]\|. \end{aligned}$$

To bound the term $\|\mathcal{F}_{\mathbf{j}}[\rho(t_n)] - \mathcal{F}_{\mathbf{j}}[\tilde{\rho}_n]\|$, we first list a generalization of the mean value theorem to complex-valued functions.

Let G be an open subset of \mathbb{R}^n , and let $f : G \rightarrow \mathbb{C}$ be a holomorphic function on G . Fix points $\mathbf{x}, \mathbf{y} \in G$ such that the line segment connecting \mathbf{x} and \mathbf{y} lies entirely within G . There exists $c_1, c_2 \in (0, 1)$ such that

$$(3.15) \quad f(\mathbf{y}) - f(\mathbf{x}) = \operatorname{Re} \left(\nabla f((1 - c_1)\mathbf{x} + c_1\mathbf{y})(\mathbf{y} - \mathbf{x}) \right) + i \operatorname{Im} \left(\nabla f((1 - c_2)\mathbf{x} + c_2\mathbf{y})(\mathbf{y} - \mathbf{x}) \right).$$

The proof of (3.15) is direct. First, we define the function

$$(3.16) \quad g(t) = f((1 - t)\mathbf{x} + t\mathbf{y}), \quad t \in [0, 1].$$

Then g is also a holomorphic function. Then, by the mean value theorem, there exist points $c_1, c_2 \in (0, 1)$ such that,

$$(3.17) \quad \operatorname{Re}(g'(c_1)) = \operatorname{Re}(g(1) - g(0)) \quad \operatorname{Im}(g'(c_2)) = \operatorname{Im}(g(1) - g(0)),$$

which implies Eq. (3.15). Applying this result to $f(\mathbf{x}) = e^{-i\omega_{\mathbf{j}}\mathbf{x}}$, we obtain:

$$(3.18) \quad \begin{aligned} \|e^{-i\omega_{\mathbf{j}}\tilde{X}_{t_n}^p} - e^{-i\omega_{\mathbf{j}}X_{t_n}^p}\| &\leq \|\omega_{\mathbf{j}} \cdot \sin(\omega_{\mathbf{j}}((1 - c_1)\tilde{X}_{t_n}^p + c_1X_{t_n}^p)) \\ &\quad + i\omega_{\mathbf{j}} \cdot \cos(\omega_{\mathbf{j}}((1 - c_2)\tilde{X}_{t_n}^p + c_2X_{t_n}^p))\| \cdot \|\tilde{X}_{t_n}^p - X_{t_n}^p\| \\ &\leq \sqrt{2}\|\omega_{\mathbf{j}}\| \cdot \|\tilde{X}_{t_n}^p - X_{t_n}^p\|. \end{aligned}$$

Based on Eq. (3.18), we have

$$(3.19) \quad \|\mathcal{F}_{\mathbf{j}}[\rho(t_n)] - \mathcal{F}_{\mathbf{j}}[\tilde{\rho}_n]\| \leq \left\| \frac{\delta t M_0}{\epsilon} \sum_{p=1}^P (e^{-i\omega_{\mathbf{j}}X_{t_n}^p} - e^{-i\omega_{\mathbf{j}}\tilde{X}_{t_n}^p}) \right\| \leq \sqrt{2}M_0\|\omega_{\mathbf{j}}\| \sum_{p=1}^P \frac{\|\tilde{X}_{t_n}^p - X_{t_n}^p\|}{P}.$$

Let $Y_p = \|\tilde{X}_{t_n}^p - X_{t_n}^p\|$, where $\{Y_p\}_{p=1}^P$ are i.i.d. random variables. This follows from the fact that the particles $\{X_{t_n}^p\}_{p=1}^P$ and $\{\tilde{X}_{t_n}^p\}_{p=1}^P$ are separately i.i.d. Specifically, the i.i.d. property of $\{\tilde{X}_{t_n}^p\}_{p=1}^P$ is ensured by the RBM described in Alg. 2.2. Based on Assumption 1, Y_p is bounded. The empirical mean is defined as $\bar{Y}_P = \frac{1}{P} \sum_{p=1}^P Y_p$ and the expectation of Y_p is $\mu = \mathbb{E}[Y_p] = \mathbb{E}[\|\tilde{X}_{t_n} - X_{t_n}\|]$.

According to Bernstein's inequality, for i.i.d. random variables Y_1, Y_2, \dots, Y_P with $|Y_p - \mu| \leq M_1$ (from Assumption 1) almost surely, the probability that the empirical mean deviates from the expectation is bounded as

$$(3.20) \quad \mathbb{P}(|\bar{Y}_P - \mu| \geq \eta) \leq 2 \exp \left(-\frac{P\eta^2}{2\sigma^2 + \frac{2M_1\eta}{3}} \right),$$

where $\sigma^2 = \mathbb{E}[(Y_p - \mu)^2] \leq M_1^2$. With high probability (e.g., $1 - \delta$ for very small $\delta > 0$), the following estimate holds

$$(3.21) \quad |\bar{Y}_P - \mu| \leq \sqrt{\frac{2\sigma^2 \ln(2/\delta)}{P}} + \frac{2M_1 \ln(2/\delta)}{3P}.$$

This implies that, with probability $1 - \delta$,

$$(3.22) \quad \|\mathcal{F}_j[\rho(t_n)] - \mathcal{F}_j[\tilde{\rho}_n]\| \leq \sqrt{2}M_0\|\omega_j\| \left(\mathbb{E}[\|\tilde{X}_{t_n} - X_{t_n}\|] + \sqrt{\frac{2\sigma^2 \ln(2/\delta)}{P}} + \frac{2M_1 \ln(2/\delta)}{3P} \right).$$

Combining Eqs. (3.12)(3.14)(3.22) above, we conclude that, with high probability

$$\|\tilde{\alpha}_{t_n;j} - \alpha_{t_n;j}\| \leq \|\tilde{\alpha}_{t_{n-1};j} - \alpha_{t_{n-1};j}\| + C_1\delta t^2 + \frac{C_2\|\omega_j\|\delta t}{\sqrt{P}} + C_3\|\omega_j\|\delta t\mathbb{E}[\|\tilde{X}_{t_n} - X_{t_n}\|],$$

where $C_2 = 2\sqrt{\ln(2/\delta)}M_0^2 + \frac{2M_0M_1\ln(2/\delta)}{3}$ and $C_3 = \frac{\sqrt{2}M_0}{\epsilon}$ are constants. \square

The error estimate between ∇c and $\nabla \tilde{c}$ is more complex than that between c and \tilde{c} . To analyze this, we introduce an intermediate quantity ∇c^* . Using the frequency notation ω_j from Lemma 3.4, where $\omega_j = (\frac{2\pi j_1}{L}, \frac{2\pi j_2}{L}, \frac{2\pi j_3}{L})$, we define

$$(3.23) \quad \begin{aligned} \nabla c^*(\mathbf{x}, t_n) &:= \sum_{j \in \mathcal{H}} i\omega_j \tilde{\alpha}_{n;j} \exp(i\omega_j \mathbf{x}) \\ &= -\frac{\epsilon}{\delta t} \int \nabla_{\mathbf{x}} \mathcal{K}_{\epsilon, \delta t}(\mathbf{x} - \mathbf{y}) \tilde{c}_{n-1}(\mathbf{y}) d\mathbf{y} - \sum_{q=1}^P \frac{M_0}{P} \nabla_{\mathbf{x}} \mathcal{K}_{\epsilon, \delta t}(\mathbf{x} - \tilde{X}_n^q) \\ &= -\frac{\epsilon}{\delta t} \underbrace{\int \nabla_{\mathbf{x}} \mathcal{K}_{\epsilon, \delta t}(\mathbf{x} + \bar{\mathbf{x}} - \mathbf{y}) \tilde{c}_{n-1}(\mathbf{y} - \bar{\mathbf{x}}) d\mathbf{y}}_{I_1} - \underbrace{\sum_{q=1}^P \frac{M_0}{P} \nabla_{\mathbf{x}} \mathcal{K}_{\epsilon, \delta t}(\mathbf{x} - \tilde{X}_n^q)}_{I_2}, \end{aligned}$$

where $\bar{\mathbf{x}} = \frac{L}{2H} + \lfloor \frac{\mathbf{x}}{L/H} \rfloor \frac{L}{H} - \mathbf{x}$. From Alg. 2.2, it follows that

$$(3.24) \quad \begin{aligned} \nabla \tilde{c}(\mathbf{x}, t_n) &= -\nabla_{\mathbf{x}} \mathcal{K}_{\epsilon, \delta t} * (\epsilon \tilde{c}_{n-1}(\mathbf{x}) / \delta t + \tilde{\rho}_n(\mathbf{x})) \\ &= -\frac{\epsilon}{\delta t} \frac{L^3}{H^3} \underbrace{\sum_{j \in \mathcal{H}} \nabla_{\mathbf{x}} \mathcal{K}_{\epsilon, \delta t}(\mathbf{x} + \bar{\mathbf{x}} - x_j) \tilde{c}_{n-1}(x_j - \bar{\mathbf{x}})}_{I_3} \\ &\quad - \underbrace{\sum_{s \in C_p, s \neq p} \frac{M_0}{R} \nabla_{\mathbf{x}} \mathcal{K}_{\epsilon, \delta t}(\mathbf{x} - \tilde{X}_n^s)}_{I_4}, \end{aligned}$$

where $x_j = (\frac{j_1 L}{H}, \frac{j_2 L}{H}, \frac{j_3 L}{H})$. The error between ∇c and $\nabla \tilde{c}$ can be estimated by

$$(3.25) \quad \|\nabla c(\mathbf{x}, t_n) - \nabla \tilde{c}(\mathbf{x}, t_n)\| \leq \|\nabla c(\mathbf{x}, t_n) - \nabla c^*(\mathbf{x}, t_n)\| + \|\nabla c^*(\mathbf{x}, t_n) - \nabla \tilde{c}(\mathbf{x}, t_n)\|.$$

To estimate the error between $\nabla \tilde{c}$ and ∇c^* , we divide the analysis into two parts:

$$(3.26) \quad \|\nabla \tilde{c}(\mathbf{x}, t_n) - \nabla c^*(\mathbf{x}, t_n)\| \leq \frac{\epsilon}{\delta t} \|I_1 - I_3\| + \|I_2 - I_4\|.$$

The first part, involving I_1 and I_3 , focuses on the different methods of approximating $(\nabla_{\mathbf{x}}\mathcal{K}_{\epsilon,\delta t} * \tilde{c})$ in $\nabla\tilde{c}$ and ∇c^* , while the second part, involving I_2 and I_4 , examines the differences in the approximations of $(\nabla_{\mathbf{x}}\mathcal{K}_{\epsilon,\delta t} * \tilde{\rho})$ between $\nabla\tilde{c}$ and ∇c^* . Specifically, I_1 represents the continuous integral, while I_3 is constructed as a discrete Riemann sum that approximates this integral, excluding the interval $[-\frac{L}{2H}, \frac{L}{2H}]^3$.

To analyze the error introduced by the approximation of $(\nabla_{\mathbf{x}}\mathcal{K}_{\epsilon,\delta t} * \tilde{c})$, we rely on the following lemma.

LEMMA 3.5. *For all $n \in \mathbb{N}_+$, under Assumption 2, based on the definitions of I_1 and I_3 given in Eq. (3.23) and Eq. (3.24), the following error bound holds:*

$$(3.27) \quad \|I_1 - I_3\| \leq \frac{C_4}{H^2} + C_5\delta t,$$

where C_4 and C_5 are constants, and $t_n = n\delta t$.

Proof. We rewrite the integral as follows to facilitate the computation of the error between I_1 and I_3 . Specifically, we have

$$(3.28) \quad \begin{aligned} I_1 = & \underbrace{\int_{\mathbf{x}+\bar{\mathbf{x}}-\mathbf{y} \in [-\frac{L}{2H}, \frac{L}{2H}]^3} \nabla_{\mathbf{x}}\mathcal{K}_{\epsilon,\delta t}(\mathbf{x} + \bar{\mathbf{x}} - \mathbf{y})\tilde{c}_{n-1}(\mathbf{y} - \bar{\mathbf{x}}) d\mathbf{y}}_{I_{1,1}} \\ & + \underbrace{\int_{\mathbf{x}+\bar{\mathbf{x}}-\mathbf{y} \in [-\frac{L}{2}, \frac{L}{2}]^3 \setminus [-\frac{L}{2H}, \frac{L}{2H}]^3} \nabla_{\mathbf{x}}\mathcal{K}_{\epsilon,\delta t}(\mathbf{x} + \bar{\mathbf{x}} - \mathbf{y})\tilde{c}_{n-1}(\mathbf{y} - \bar{\mathbf{x}}) d\mathbf{y}}_{I_{1,2}}. \end{aligned}$$

The leading-order term of the error $\|I_3 - I_{1,2}\|$ depends on the smoothness of the integrand, in particular, the second derivatives of the product of functions $\nabla_{\mathbf{x}}\mathcal{K}_{\epsilon,\delta t}$ and \tilde{c}_{n-1} . Under Assumption 2 (a), \tilde{c}_{n-1} is assumed to be twice continuously differentiable, with its derivatives uniformly bounded. Furthermore, with the inclusion of the shift term, $\nabla_{\mathbf{x}}\mathcal{K}_{\epsilon,\delta t}$ can be regarded as smooth, similar to $I_{1,2}$. The smoothness of $\nabla_{\mathbf{x}}\mathcal{K}_{\epsilon,\delta t}$ and \tilde{c}_{n-1} in $[-\frac{L}{2}, \frac{L}{2}]^3 \setminus [-\frac{L}{2H}, \frac{L}{2H}]^3$ ensures that the integrand is twice differentiable, and its second derivatives are uniformly bounded. As a result, the error $\|I_3 - I_{1,2}\|$ can be bounded by:

$$(3.29) \quad \|I_3 - I_{1,2}\| \leq \frac{C_4}{H^2},$$

where the constant C_4 satisfies that $C_4 = (M_3 + K)L^2$. The boundedness of C_4 is a combined outcome of the derivation, as it relies on the uniform bounds of the second derivatives of the integrand, which follows from the smoothness of $\nabla_{\mathbf{x}}\mathcal{K}_{\epsilon,\delta t}$ in $[-\frac{L}{2}, \frac{L}{2}]^3 \setminus [-\frac{L}{2H}, \frac{L}{2H}]^3$, combined with the regularity of \tilde{c}_{n-1} given by Assumption 2(a) and (c).

The integral $I_{1,1}$ is defined as:

$$\begin{aligned}
I_{1,1} &= \int_{\mathbf{z} \in [-\frac{L}{2H}, \frac{L}{2H}]^3} \nabla_{\mathbf{x}} \mathcal{K}_{\epsilon, \delta t}(\mathbf{z}) \tilde{c}_{n-1}(\mathbf{x} - \mathbf{z}) d\mathbf{z} \\
&= \underbrace{\tilde{c}_{n-1}(\mathbf{x}) \int \nabla_{\mathbf{x}} \mathcal{K}_{\epsilon, \delta t}(\mathbf{z}) d\mathbf{z}}_{I_{1,1}^{(0)}} - \underbrace{\int \nabla_{\mathbf{x}} \mathcal{K}_{\epsilon, \delta t}(\mathbf{z}) (\nabla \tilde{c}_{n-1}(\mathbf{x}) \cdot \mathbf{z}) d\mathbf{z}}_{I_{1,1}^{(1)}} \\
(3.30) \quad &+ \underbrace{\frac{1}{2} \int \nabla_{\mathbf{x}} \mathcal{K}_{\epsilon, \delta t}(\mathbf{z}) (\mathbf{z}^\top H(\tilde{c}_{n-1}(\xi)) \mathbf{z}) d\mathbf{z}}_{R_1},
\end{aligned}$$

where $H(\tilde{c}_{n-1}(\xi))$ is the Hessian matrix of \tilde{c}_{n-1} (composed of second-order partial derivatives at some point ξ between \mathbf{z} and \mathbf{x}).

Since $\int_{\mathbf{z}} \mathbf{z} d\mathbf{z} = 0$ over a symmetric domain, the zeroth-order term $I_{1,1}^{(0)}$ vanishes:

$$(3.31) \quad I_{1,1}^{(0)} = \tilde{c}_{n-1}(\mathbf{x}) \int_{\mathbf{z}} \frac{\exp(-\beta \|\mathbf{z}\|)}{4\pi \|\mathbf{z}\|^3} (1 + \beta \|\mathbf{z}\|) \mathbf{z} d\mathbf{z} = 0,$$

where $\beta = \sqrt{\lambda^2 + \epsilon/\delta t}$ is the same parameter as defined in Eq. (2.9).

For the first term $I_{1,1}^{(1)}$, switching to spherical coordinates: let $\|\mathbf{z}\| = r$, $\mathbf{z} = r\hat{\mathbf{z}}$, where $\hat{\mathbf{z}}$ is the unit vector $(\sin \theta \cos \phi, \sin \theta \sin \phi, \cos \theta)$. Substituting these, the integral becomes:

$$\begin{aligned}
\|I_{1,1}^{(1)}\| &\leq \left\| - \int_0^{\frac{L}{2H}} \int_0^\pi \int_0^{2\pi} \frac{\exp(-\beta r)}{4\pi r^3} (1 + \beta r) r^4 \hat{\mathbf{z}} (\hat{\mathbf{z}} \cdot \nabla \tilde{c}_{n-1}(\mathbf{x})) \sin \theta d\phi d\theta dr \right\| \\
&= \left\| - \frac{\nabla \tilde{c}_{n-1}(\mathbf{x})}{\beta^2} \left[1 - \left(1 + \beta \frac{L}{2H} + \frac{1}{3} \left(\beta \frac{L}{2H} \right)^2 \right) \exp\left(-\beta \frac{L}{2H}\right) \right] \right\| \\
(3.32) \quad &\leq \left| \frac{M_3}{\beta^2} \right|,
\end{aligned}$$

where, according to Assumption 2(c), M_3 is the uniform bound of $\nabla \tilde{c}_{n-1}$.

Under Assumption 2(a), $H(\tilde{c}_{n-1}(\xi))$ is bounded, and thus we can get the inequality for the remainder term R_1 :

$$\begin{aligned}
|R_1| &\leq \left| \frac{1}{2} \int_0^{\frac{L}{2H}} \int_0^\pi \int_0^{2\pi} \frac{\exp(-\beta r)}{4\pi r^3} (1 + \beta r) \cdot r^2 (\hat{\mathbf{z}}^\top H(\tilde{c}_{n-1}(\xi)) \hat{\mathbf{z}}) \cdot r^2 \sin \theta d\phi d\theta dr \right| \\
&\leq \left| \frac{K}{6} \int_0^{\frac{L}{2H}} r \exp(-\beta r) (1 + \beta r) dr \right| \\
(3.33) \quad &\leq \frac{K}{2\beta^2},
\end{aligned}$$

where K is the spatial Lipschitz constant for $\nabla \tilde{c}$ defined in Assumption 2(a).

From the above inequalities, we can conclude that:

$$(3.34) \quad \|I_1 - I_3\| \leq \frac{C_4}{H^2} + C_5 \delta t,$$

where $C_5 = \frac{2M_3 + K}{2\epsilon}$ is a constant. \square

We now estimate $(\nabla_{\mathbf{x}}\mathcal{K}_{\epsilon,\delta t} * \tilde{\rho}_n)(\tilde{X}_n^p)$ in $\nabla\tilde{c}$ and ∇c^* . Using the RBM in Alg. 2.2, we replace $\sum_{q=1, q \neq p}^P \frac{M_0}{P} \nabla_{\mathbf{x}}\mathcal{K}_{\epsilon,\delta t}(\tilde{X}_n^p - \tilde{X}_n^q)$ with $\sum_{s \in C_p, s \neq p} \frac{M_0}{R} \nabla_{\mathbf{x}}\mathcal{K}_{\epsilon,\delta t}(\tilde{X}_n^p - \tilde{X}_n^s)$. We write

$$(3.35) \quad \zeta_{n,p} := \sum_{q=1, q \neq p}^P \frac{M_0}{P} \nabla_{\mathbf{x}}\mathcal{K}_{\epsilon,\delta t}(\tilde{X}_n^p - \tilde{X}_n^q) - \sum_{s \in C_p, s \neq p} \frac{M_0}{R} \nabla_{\mathbf{x}}\mathcal{K}_{\epsilon,\delta t}(\tilde{X}_n^p - \tilde{X}_n^s).$$

LEMMA 3.6. *For $\forall n \in \mathbb{N}_+$, $p \in \{1, 2, \dots, P\}$, we have the estimate as follows:*

$$(3.36) \quad \mathbb{E}(\|\zeta_{n,p}\|) \leq M_0 M_4 \sqrt{\left(\frac{1}{R} - \frac{1}{P}\right)},$$

where $M_4 = \max_{q \neq p} \|\nabla_{\mathbf{x}}\mathcal{K}_{\epsilon,\delta t}(\tilde{X}_n^p - \tilde{X}_n^q)\|$, M_0 is the conserved total mass, P is the total number of particles, and R is the batch size.

Proof. Similar to Lemma 3.1 in [17], we rewrite

$$(3.37) \quad f_p = \sum_{s \in C_p, s \neq p} \frac{M_0}{R} \nabla_{\mathbf{x}}\mathcal{K}_{\epsilon,\delta t}(\tilde{X}_n^p - \tilde{X}_n^s) = \sum_{q=1, q \neq p}^P \frac{M_0}{R} \nabla_{\mathbf{x}}\mathcal{K}_{\epsilon,\delta t}(\tilde{X}_n^p - \tilde{X}_n^q) I(p, q),$$

where $I(p, q)$ denotes that q belongs to the batch C_p . Here we have that $I(p, q)$ is a Bernoulli random variable with $\mathbb{E}[I(p, q)] = \frac{R}{P}$, which indicates that $\mathbb{E}[\zeta_{n,p}] = 0$.

$$\begin{aligned} \mathbb{E}|f_p|^2 &= \frac{M_0^2}{R^2} \sum_{\substack{q,r: \\ q \neq r, q \neq p, \\ r \neq p}} \|\nabla_{\mathbf{x}}\mathcal{K}_{\epsilon,\delta t}(\tilde{X}_n^p - \tilde{X}_n^q) \cdot \nabla_{\mathbf{x}}\mathcal{K}_{\epsilon,\delta t}(\tilde{X}_n^p - \tilde{X}_n^r)\|^2 P(I(p, q)I(p, r) = 1) \\ &\quad + \frac{M_0^2}{R^2} \sum_{q=1, q \neq p}^P \|\nabla_{\mathbf{x}}\mathcal{K}_{\epsilon,\delta t}(\tilde{X}_n^p - \tilde{X}_n^q)\|^2 P(I(p, q) = 1) \\ &= \frac{M_0^2}{RP} \sum_{q=1, q \neq p}^P \|\nabla_{\mathbf{x}}\mathcal{K}_{\epsilon,\delta t}(\tilde{X}_n^p - \tilde{X}_n^q)\|^2 \\ &\quad + \frac{M_0^2}{P^2} \sum_{q,r: q \neq r, q \neq p, r \neq p} \|\nabla_{\mathbf{x}}\mathcal{K}_{\epsilon,\delta t}(\tilde{X}_n^p - \tilde{X}_n^q) \cdot \nabla_{\mathbf{x}}\mathcal{K}_{\epsilon,\delta t}(\tilde{X}_n^p - \tilde{X}_n^r)\|^2. \end{aligned}$$

Hence,

$$(3.38) \quad \text{Var}(\zeta_{n,p}) = \mathbb{E}|f_p|^2 - (\mathbb{E}|f_p|)^2 = M_0^2 \left(\frac{1}{R} - \frac{1}{P}\right) \frac{1}{P} \sum_{q=1, q \neq p}^P \|\nabla_{\mathbf{x}}\mathcal{K}_{\epsilon,\delta t}(\tilde{X}_n^p - \tilde{X}_n^q)\|^2.$$

According to Jensen's Inequality, we obtain:

$$(3.39) \quad \mathbb{E}(\|\zeta_{n,p}\|) \leq \sqrt{\mathbb{E}(\|\zeta_{n,p}\|^2)} = \sqrt{\text{Var}(\zeta_{n,p})} \leq M_0 M_4 \sqrt{\left(\frac{1}{R} - \frac{1}{P}\right)},$$

where $M_4 = \max_{q \neq p} \|\nabla_{\mathbf{x}}\mathcal{K}_{\epsilon,\delta t}(\tilde{X}_n^p - \tilde{X}_n^q)\|$. Since all particles are located at distinct positions in the SIPF- r algorithm ($\tilde{X}_n^p \neq \tilde{X}_n^q$ for $p \neq q$), there exists a minimum separation distance $d_{\min} > 0$ between any two distinct particles. Consequently, $\|\nabla_{\mathbf{x}}\mathcal{K}_{\epsilon,\delta t}(\tilde{X}_n^p - \tilde{X}_n^q)\|$ is bounded for all pairs of particles. This ensures that M_4 , which is the maximum of these kernel gradient norms, is finite. \square

Now we analyze the error between ∇c^* and ∇c as follows.

LEMMA 3.7. *For all $n \in \mathbb{N}_+$, under Assumption 2, with high probability, the error between the intermediate gradient ∇c^* and the exact gradient ∇c satisfies*

$$(3.40) \quad \begin{aligned} \|\nabla c^*(\mathbf{x}, t_n) - \nabla c(\mathbf{x}, t_n)\| &\leq \|\nabla c^*(\mathbf{x}, t_{n-1}) - \nabla c(\mathbf{x}, t_{n-1})\| + C_6 \sqrt{\frac{\delta t}{P}} \\ &\quad + C_7 \sqrt{\delta t} \cdot \mathbb{E}[\|\tilde{X}_{t_n} - X_{t_n}\|] + C_1 \delta t^2, \end{aligned}$$

where C_1, C_6 and C_7 are constants, and $t_n = n\delta t$.

Proof. By Parseval's identity, the L^2 -norm of the gradient error is isometric to the weighted l^2 -norm of the difference in Fourier coefficients. Let $\mathbf{g}_{n;\mathbf{j}} := i\omega_{\mathbf{j}}(\alpha_{t_n;\mathbf{j}} - \tilde{\alpha}_{t_n;\mathbf{j}})$ denote the Fourier coefficient of the gradient error $\nabla c(\cdot, t_n) - \nabla c^*(\cdot, t_n)$. We have

$$(3.41) \quad \|\nabla c(\cdot, t_n) - \nabla c^*(\cdot, t_n)\| = \left(\frac{L^3}{H^3} \sum_{\mathbf{j} \in \mathcal{H}} \|\mathbf{g}_{n;\mathbf{j}}\|^2 \right)^{1/2}.$$

Recalling the recursive updates for $\alpha_{t_n;\mathbf{j}}$ and $\tilde{\alpha}_{t_n;\mathbf{j}}$ derived in Lemma 3.4, we can decompose the error $\mathbf{g}_{n;\mathbf{j}}$ into three distinct components as follows:

$$(3.42) \quad \mathbf{g}_{n;\mathbf{j}} = \frac{i\omega_{\mathbf{j}}}{1 + Z_{\mathbf{j}}} \left[(\alpha_{t_{n-1};\mathbf{j}} - \tilde{\alpha}_{t_{n-1};\mathbf{j}}) + \frac{\delta t}{\epsilon} (\mathcal{F}_{\mathbf{j}}[\rho_n] - \mathcal{F}_{\mathbf{j}}[\tilde{\rho}_n]) + \delta t \mathcal{F}_{\mathbf{j}}[R_n] \right],$$

where $Z_{\mathbf{j}} = (\|\omega_{\mathbf{j}}\|^2 + \lambda^2)\delta t/\epsilon$, and $R_n(\mathbf{x}) = -\frac{1}{\delta t} \int_{t_{n-1}}^{t_n} (s - t_{n-1}) \partial_t^2 c(\cdot, s) ds$.

Since $Z_{\mathbf{j}} > 0$, we have

$$(3.43) \quad \left\| \frac{i\omega_{\mathbf{j}}}{1 + Z_{\mathbf{j}}} (\alpha_{t_{n-1};\mathbf{j}} - \tilde{\alpha}_{t_{n-1};\mathbf{j}}) \right\| \leq \sqrt{\frac{L^3}{H^3} \sum_{\mathbf{j} \in \mathcal{H}} \|\mathbf{g}_{n-1;\mathbf{j}}\|^2} = \|\nabla c(\cdot, t_{n-1}) - \nabla c^*(\cdot, t_{n-1})\|.$$

The noise term from the particle approximation in Lemma 3.4 contributes to the gradient error as

$$(3.44) \quad \left\| \frac{i\omega_{\mathbf{j}}\delta t}{\epsilon(1 + Z_{\mathbf{j}})} (\mathcal{F}_{\mathbf{j}}[\rho_n] - \mathcal{F}_{\mathbf{j}}[\tilde{\rho}_n]) \right\| \leq \frac{\|\omega_{\mathbf{j}}\|\delta t}{\epsilon + \delta t(\|\omega_{\mathbf{j}}\|^2 + \lambda^2)} \left(\frac{C_2}{\sqrt{P}} + \sqrt{2}M_0 \mathbb{E}[\|\tilde{X}_{t_n} - X_{t_n}\|] \right),$$

where $C_2 = 2\sqrt{\ln(2/\delta)}M_0^2 + \frac{2M_0M_1 \ln(2/\delta)}{3}$ is a constant. Define the function $f(k) = \frac{k\delta t}{\epsilon + \delta t(k^2 + \lambda^2)}$. The maximum of $f(k)$ for $k \geq 0$ satisfies

$$(3.45) \quad \sup_{k \geq 0} f(k) \leq \frac{\delta t}{2\sqrt{\epsilon}\delta t} = \frac{1}{2} \sqrt{\frac{\delta t}{\epsilon}}.$$

Then, we get that

$$(3.46) \quad \left\| i\omega_{\mathbf{j}} \frac{\delta t/\epsilon}{1 + Z_{\mathbf{j}}} (\mathcal{F}_{\mathbf{j}}[\rho_n] - \mathcal{F}_{\mathbf{j}}[\tilde{\rho}_n]) \right\| \leq \frac{1}{2} \sqrt{\frac{\delta t}{\epsilon}} \left(\frac{C_2}{\sqrt{P}} + \sqrt{2}M_0 \mathbb{E}[\|\tilde{X}_{t_n} - X_{t_n}\|] \right).$$

For the term $\frac{i\omega_{\mathbf{j}}}{1+Z_{\mathbf{j}}}\delta t\mathcal{F}_{\mathbf{j}}[R_n]$, we have

$$(3.47) \quad \left\| \frac{i\omega_{\mathbf{j}}}{1+Z_{\mathbf{j}}}\delta t\mathcal{F}_{\mathbf{j}}[R_n] \right\| \leq \delta t \sqrt{\frac{L^3}{H^3} \sum_{\mathbf{j} \in \mathcal{H}} \|i\omega_{\mathbf{j}}\mathcal{F}_{\mathbf{j}}[R_n]\|^2} = \delta t \|\nabla R_n(\mathbf{x})\|.$$

Recalling the definition $R_n(\mathbf{x}) = -\frac{1}{\delta t} \int_{t_{n-1}}^{t_n} (s - t_{n-1}) \partial_t^2 c(\cdot, s) ds$, we have

$$(3.48) \quad \|\nabla R_n\| \leq \frac{1}{\delta t} \int_{t_{n-1}}^{t_n} (s - t_{n-1}) \|\nabla \partial_t^2 c(\cdot, s)\| ds \leq \frac{\delta t}{2} \sup_{s \in [t_{n-1}, t_n]} \|\nabla \partial_t^2 c(\cdot, s)\|.$$

By Assumption 2(d), $\|\nabla \partial_t^2 c\|$ is bounded by K_2 . Thus, we can get that

$$(3.49) \quad \left\| \frac{i\omega_{\mathbf{j}}}{1+Z_{\mathbf{j}}}\delta t\mathcal{F}_{\mathbf{j}}[R_n] \right\| \leq \frac{K_2}{2} \delta t^2.$$

Summing over $\mathbf{j} \in \mathcal{H}$ and applying the Minkowski inequality, we obtain

$$(3.50) \quad \begin{aligned} \|\nabla c^*(\mathbf{x}, t_n) - \nabla c(\mathbf{x}, t_n)\| &\leq \|\nabla c^*(\mathbf{x}, t_{n-1}) - \nabla c(\mathbf{x}, t_{n-1})\| + C_6 \sqrt{\frac{\delta t}{P}} \\ &\quad + C_7 \sqrt{\delta t} \cdot \mathbb{E}[\|\tilde{X}_{t_n} - X_{t_n}\|] + C_1 \delta t^2, \end{aligned}$$

where $C_1 = \frac{K_2}{2}$, $C_6 = \frac{3\sqrt{\ln(2/\delta)}M_0^2 + M_0M_1 \ln(2/\delta)}{3\sqrt{\epsilon}}$, and $C_7 = \frac{M_0}{\sqrt{2\epsilon}}$. \square

Hence, combining Lemmas 3.5, 3.6, 3.7, and Eq. (3.25), we get that with high probability:

$$(3.51) \quad \begin{aligned} \mathbb{E}(\|\nabla c(\tilde{X}_{t_n}, t_n) - \nabla \tilde{c}(\tilde{X}_{t_n}, t_n)\|) &\leq \frac{\epsilon}{\delta t} \left(\frac{C_4}{H^2} + C_5 \delta t \right) + C_1 \delta t^2 + C_7 \sqrt{\delta t} \cdot \mathbb{E}[\|\tilde{X}_{t_n} - X_{t_n}\|] \\ &\quad + \mathbb{E}(\|\nabla c^*(\mathbf{x}, t_{n-1}) - \nabla c(\mathbf{x}, t_{n-1})\|) + C_6 \sqrt{\frac{\delta t}{P}}. \end{aligned}$$

3.3. Proof of the Main Theorem. Building on the lemmas established in the previous subsection, we now prove the main theorem in this section. For simplicity of notation in the proof below, we define:

$$(3.52) \quad a_n := \mathbb{E}(\|\tilde{X}_{t_n} - X_{t_n}\|),$$

$$(3.53) \quad b_n := \mathbb{E}(\|\nabla c(\tilde{X}_{t_n}, t_n) - \nabla c^*(\tilde{X}_{t_n}, t_n)\|).$$

The following provides a bound on the error between $\tilde{X}_{t_{n+1}}$ and $X_{t_{n+1}}$.

LEMMA 3.8. *For all $n \in \mathbb{N}_+$, under Assumption 2,*

$$(3.54) \quad \mathbb{E}(\|\tilde{X}_{t_{n+1}} - X_{t_{n+1}}\|) \leq (1 + C_8 \delta t) a_n + \chi \delta t b_n + C_9 \delta t + \frac{C_{10}}{H^2} + \frac{C_{11} \delta t}{\sqrt{R}},$$

where C_8 , C_9 , C_{10} , and C_{11} are constants, χ is the chemotaxis coefficient in the system (1.1), and $t_n = n\delta t$.

Proof. According to Eqs. (2.15)-(2.16), we can get that

$$(3.55) \quad \begin{aligned} \mathbb{E}(\|\tilde{X}_{t_{n+1}} - X_{t_{n+1}}\|) &\leq \mathbb{E}(\|\tilde{X}_{t_n} - X_{t_n}\|) + \chi \mathbb{E} \left(\int_{t_n}^{t_{n+1}} \|\nabla \tilde{c}(\tilde{X}_{t_n}, t_n) - \nabla c(X_s, s)\| ds \right) \\ &= \mathbb{E}(\|\tilde{X}_{t_n} - X_{t_n}\|) + \chi \int_{t_n}^{t_{n+1}} \mathbb{E}(\|\nabla \tilde{c}(\tilde{X}_{t_n}, t_n) - \nabla c(X_s, s)\|) ds, \end{aligned}$$

by the triangle inequality and Tonelli's theorem. According to Assumption 2(a),

$$\begin{aligned}
\|\nabla\tilde{c}(\tilde{X}_{t_n}, t_n) - \nabla c(X_s, s)\| &\leq \|\nabla\tilde{c}(\tilde{X}_{t_n}, t_n) - \nabla c(\tilde{X}_{t_n}, t_n)\| + \|\nabla c(\tilde{X}_{t_n}, t_n) - \nabla c(X_{t_n}, t_n)\| \\
&\quad + \|\nabla c(X_{t_n}, t_n) - \nabla c(X_s, s)\| \\
&\leq \|\nabla\tilde{c}(\tilde{X}_{t_n}, t_n) - \nabla c(\tilde{X}_{t_n}, t_n)\| + K\|X_{t_n} - \tilde{X}_{t_n}\| \\
&\quad + \|\nabla c(X_{t_n}, t_n) - \nabla c(X_s, s)\|,
\end{aligned}
\tag{3.56}$$

where K is the Lipschitz constant defined in Assumption 2(a). Using the notations for a_n and b_n in Eqs. (3.52)-(3.53), we can obtain the estimate as follows:

$$\begin{aligned}
a_{n+1} &= \mathbb{E}(\|\tilde{X}_{t_{n+1}} - X_{t_{n+1}}\|) \\
&\leq \mathbb{E}(\|\tilde{X}_{t_n} - X_{t_n}\|) + \chi \int_{t_n}^{t_{n+1}} \mathbb{E}(\|\nabla\tilde{c}(\tilde{X}_{t_n}, t_n) - \nabla c(\tilde{X}_{t_n}, t_n)\|) ds \\
&\quad + \chi K \int_{t_n}^{t_{n+1}} \mathbb{E}(\|\tilde{X}_{t_n} - X_{t_n}\|) ds + \chi \int_{t_n}^{t_{n+1}} \mathbb{E}(\|\nabla c(X_{t_n}, t_n) - \nabla c(X_s, s)\|) ds \\
&\leq (1 + \chi K \delta t) a_n + \chi \int_{t_n}^{t_{n+1}} \mathbb{E}(\|\nabla c(X_{t_n}, t_n) - \nabla c(X_s, s)\|) ds \\
&\quad + \chi \delta t \left(b_n + \frac{\epsilon}{\delta t} \left(\frac{C_4}{H^2} + C_5 \delta t \right) + M_0 M_4 \sqrt{\left(\frac{1}{R} - \frac{1}{P} \right)} \right) \\
&\leq (1 + \chi K \delta t) a_n + \chi \delta t b_n \\
&\quad + \chi \delta t \left(2M_3 + \frac{\epsilon}{\delta t} \left(\frac{C_4}{H^2} + C_5 \delta t \right) + M_0 M_4 \sqrt{\left(\frac{1}{R} - \frac{1}{P} \right)} \right) \\
&\leq (1 + C_8 \delta t) a_n + \chi \delta t b_n + C_9 \delta t + \frac{C_{10}}{H^2} + \frac{C_{11} \delta t}{\sqrt{R}},
\end{aligned}
\tag{3.57}$$

where the constants are defined as $C_8 = \chi K$, $C_9 = 2\chi M_3 + \epsilon\chi C_5$, $C_{10} = \epsilon\chi C_4$, and $C_{11} = \chi M_0 M_4$. This concludes the proof. \square

Finally, we are ready to prove Theorem 3.2.

Proof of Theorem 3.2. From Lemma 3.8 and Eq. (3.51), we obtain the system of inequalities that couples a_n and b_n defined in Eqs. (3.52)-(3.53) as follows:

$$a_{n+1} \leq (1 + C_8 \delta t) a_n + \chi \delta t b_n + C_9 \delta t + \frac{C_{10}}{H^2} + \frac{C_{11} \delta t}{\sqrt{R}},
\tag{3.58}$$

$$b_{n+1} \leq b_n + \frac{C_{10}}{H^2} + C_6 \sqrt{\frac{\delta t}{P}} + C_7 \sqrt{\delta t} a_{n+1} + C_1 \delta t^2.
\tag{3.59}$$

From this coupled system, we can derive a general bound for a_n . To be specific, substituting Eq. (3.59) into Eq. (3.58), we iteratively propagate and simplify the inequality to derive:

$$\begin{aligned}
a_{n+1} &\leq (1 + \delta t (C_7 \sqrt{\delta t} + C_8)) a_n + \sum_{j=1}^{n-1} C_7 \delta t^{\frac{3}{2}} a_j + (C_9 + \chi T C_1) \delta t \\
&\quad + \frac{\chi T C_{10}}{H^2} + \chi T C_6 \sqrt{\frac{\delta t}{P}} + \frac{C_{11} \delta t}{\sqrt{R}}.
\end{aligned}
\tag{3.60}$$

By the discrete Gronwall inequality, if (u_n) and (w_n) are nonnegative sequences satisfying

$$(3.61) \quad u_n \leq \alpha + \sum_{k=0}^{n-1} u_k w_k \quad \forall n \geq 1,$$

for some constant $\alpha \geq 0$. Then for all $n \geq 1$, the sequence (u_n) satisfies the bound

$$(3.62) \quad u_n \leq \alpha \exp\left(\sum_{k=0}^{n-1} w_k\right).$$

Applying this result to the recursive inequality Eq. (3.60), we obtain the following bound that holds with high-probability:

$$(3.63) \quad a_{n+1} \leq \left(\frac{N_0}{H^2} + N_1 \delta t + N_2 \sqrt{\frac{\delta t}{P}} + \frac{N_3 \delta t}{\sqrt{R}}\right) \cdot \exp(1 + N_4 \sqrt{\delta t}),$$

for all $n \geq 0$, where $N_0 = \chi TC_{10}$, $N_1 = C_9 + \chi TC_1$, $N_2 = \chi TC_6$, $N_3 = C_{11}$, and $N_4 = TC_7$. Moreover, we point out that, C_1, C_2 are constants defined in Lemma 3.4, C_6, C_7 are constants defined in Lemma 3.7, C_9, C_{10}, C_{11} are constants defined in Lemma 3.8. The higher-order terms are omitted in the leading-order bound.

According to the discrete and continuous dynamics defined in Eqs. (2.15)-(2.16), the 1-Wasserstein distance between the approximate and exact distributions at time t_{n+1} is given by:

$$(3.64) \quad \mathcal{W}_1(\tilde{\rho}_{t_{n+1}}, \rho_{t_{n+1}}) = \inf_{\gamma \in \Pi(\tilde{\rho}_{t_{n+1}}, \rho_{t_{n+1}})} \left(\int_{\mathbb{R}^3 \times \mathbb{R}^3} \|\mathbf{x} - \mathbf{y}\|_{L^1} d\gamma(\mathbf{x}, \mathbf{y}) \right),$$

where the infimum is taken over all possible couplings of the two distributions.

Under the natural coupling induced by shared initial conditions and Brownian motion paths (i.e., \tilde{X}_{t_n} and X_{t_n} evolve via the same Wiener process W_s), we explicitly construct a joint distribution $\gamma_n = \text{Law}(\tilde{X}_{t_n}, X_{t_n})$. This coupling allows us to bound the Wasserstein distance as:

$$(3.65) \quad \begin{aligned} \mathcal{W}_1(\tilde{\rho}_{t_{n+1}}, \rho_{t_{n+1}}) &\leq \mathbb{E}(\|\tilde{X}_{t_{n+1}} - X_{t_{n+1}}\|_{L^1}) \\ &\leq \sqrt{3} \mathbb{E}(\|\tilde{X}_{t_{n+1}} - X_{t_{n+1}}\|_{L^2}) \\ &\leq \left(\frac{S_0}{H^2} + S_1 \delta t + S_2 \sqrt{\frac{\delta t}{P}} + \frac{S_3 \delta t}{\sqrt{R}}\right) \cdot \exp(1 + S_4 \sqrt{\delta t}), \end{aligned}$$

where $S_0 = \sqrt{3}N_0$, $S_1 = \sqrt{3}N_1$, $S_2 = \sqrt{3}N_2$, $S_3 = \sqrt{3}N_3$, and $S_4 = N_4$. The inequality follows from the fact that the Wasserstein distance is defined as the infimum over all possible couplings, and our construction provides one such coupling. This step follows from the elementary norm inequality $\|\mathbf{x}\|_{L^1} \leq \sqrt{3}\|\mathbf{x}\|_{L^2}$ for vectors in \mathbb{R}^3 , which is a direct consequence of the Cauchy-Schwarz inequality.

To derive the bound for the Fourier coefficients in Eq. (3.8), we explicitly incorporate the Fourier mode H into the error analysis. In the proof of Lemma 3.7, the stochastic noise was uniformly bounded. Here, by utilizing the condition $\|\omega_{\mathbf{j}}\| \leq \sqrt{3}\pi H/L$ for $\mathbf{j} \in \mathcal{H}$, we can obtain a new bound for b_n as follows:

$$(3.66) \quad b_{n+1} \leq b_n + \frac{C_{12}H\delta t}{\sqrt{P}} + C_3\sqrt{\delta t}a_n + C_1\delta t^2,$$

where $C_{12} = \sqrt{3}\pi C_6/L$ is a constant. Consequently, the resulting particle error bound takes the following form:

$$(3.67) \quad a_{n+1} \leq \left(\frac{N_0}{H^2} + N_1\delta t + \frac{N_5 H \delta t}{\sqrt{P}} + \frac{N_3 \delta t}{\sqrt{R}} \right) \cdot \exp(1 + N_4 \sqrt{\delta t}),$$

where $N_5 = \chi T C_{12}$ is a constant. Finally, we sum the single-step errors from Lemma 3.4 over $n \leq \lfloor T/\delta t \rfloor$ steps (i.e., up to the final time T) using this form of a_n :

$$(3.68) \quad \begin{aligned} \max_{\mathbf{j} \in \mathcal{H}} \|\tilde{\alpha}_{t_n; \mathbf{j}} - \alpha_{t_n; \mathbf{j}}\| &\leq \sum_{k=1}^n \left(C_1 \delta t^2 + C_2 \frac{\|\omega_{\mathbf{j}}\| \delta t}{\sqrt{P}} + C_3 \|\omega_{\mathbf{j}}\| \delta t \cdot a_k \right) \\ &\leq \left(\frac{S_5}{H} + S_6 H \delta t + \frac{S_7 H^2 \delta t}{\sqrt{P}} + \frac{S_8 H \delta t}{\sqrt{R}} \right) \cdot \exp(1 + S_4 \sqrt{\delta t}) + \frac{S_9 H}{\sqrt{P}}, \end{aligned}$$

where we define $\kappa = \frac{\sqrt{3}\pi T}{L}$, $S_5 = \kappa C_3 N_0$, $S_6 = \kappa C_3 N_1$, $S_7 = \kappa C_3 N_5$, $S_8 = \kappa C_3 N_3$, and $S_9 = \kappa C_2$. Moreover, we point out that C_2 and C_3 are constants defined in Lemma 3.4. We also omit higher-order terms in the leading-order bound. This completes the proof of Theorem 3.2.

3.4. Numerical unconditional stability of the SIPF- r method. The SIPF- r method exhibits inherent numerical stability regarding the chemical concentration field. This property stems directly from the spectral discretization and the implicit time-stepping scheme, a property that is independent of the particle distribution. We establish that both the chemical concentration \tilde{c} and its gradient $\nabla \tilde{c}$ remain uniformly bounded for any fixed Fourier mode H , thereby justifying the boundedness assumptions employed in the convergence analysis.

LEMMA 3.9 (Unconditional stability of \tilde{c} and $\nabla \tilde{c}$). *Let H be the finite number of Fourier modes and Ω be the spatial domain. For any time step $n \geq 0$ and the fixed Fourier mode H , the reconstructed concentration field \tilde{c}_n and its gradient satisfy the uniform bounds:*

$$(3.69) \quad \|\tilde{c}_n\|_{L^\infty(\Omega)} \leq C_{\text{stab}} H + C_0,$$

and

$$(3.70) \quad \|\nabla \tilde{c}_n\|_{L^\infty(\Omega)} := \sup_{\mathbf{x} \in \Omega} \|\nabla \tilde{c}_n(\mathbf{x})\|_{L^2} \leq C_{\text{reg}}(H),$$

where $C_{\text{stab}}, C_0 > 0$ are constants depending only on the initial data, M_0 , λ , and the domain size L , and $C_{\text{reg}}(H)$ is a constant that depends on H , L , M_0 , and λ , but is independent of the time step size δt and the particle positions $\{\tilde{X}_n^p\}_{p=1}^P$.

Proof. The update formula for the Fourier coefficients $\tilde{\alpha}_{n; \mathbf{j}}$ in the SIPF- r algorithm is derived from the implicit Euler discretization. By rearranging the terms in Eq. (2.7) and applying the Fourier transform, the update relates $\tilde{\alpha}_{n; \mathbf{j}}$ to the previous state $\tilde{\alpha}_{n-1; \mathbf{j}}$ and the current empirical density $\hat{\rho}_{n; \mathbf{j}}$ via the amplification factor

$$(3.71) \quad \tilde{\alpha}_{n; \mathbf{j}} = \frac{1}{1 + Z_{\mathbf{j}}} \tilde{\alpha}_{n-1; \mathbf{j}} + \frac{\delta t / \epsilon}{1 + Z_{\mathbf{j}}} \hat{\rho}_{n; \mathbf{j}}, \quad \text{with } Z_{\mathbf{j}} = \frac{\delta t}{\epsilon} (\|\omega_{\mathbf{j}}\|^2 + \lambda^2).$$

The source term associated with the particles satisfies that

$$(3.72) \quad |\hat{\rho}_{n; \mathbf{j}}| = \left| \frac{M_0}{P} \sum_{p=1}^P e^{-i\omega_{\mathbf{j}} \cdot \tilde{X}_n^p} \right| \leq M_0.$$

Applying the recursive relation and the triangle inequality yields a bound via geometric series for the magnitude of the coefficients:

$$\begin{aligned}
 |\tilde{\alpha}_{n;\mathbf{j}}| &\leq \frac{1}{1+Z_{\mathbf{j}}} |\tilde{\alpha}_{n-1;\mathbf{j}}| + \frac{M_0 \delta t / \epsilon}{1+Z_{\mathbf{j}}} \\
 &\leq \left(\frac{1}{1+Z_{\mathbf{j}}} \right)^n |\tilde{\alpha}_{0;\mathbf{j}}| + \frac{M_0 \delta t}{\epsilon(1+Z_{\mathbf{j}})} \sum_{k=0}^{n-1} \left(\frac{1}{1+Z_{\mathbf{j}}} \right)^k \\
 (3.73) \quad &\leq |\tilde{\alpha}_{0;\mathbf{j}}| + \frac{M_0}{\|\omega_{\mathbf{j}}\| + \lambda^2}.
 \end{aligned}$$

We next bound $\|\tilde{c}_n\|_{L^\infty}$ by approximating the partial Fourier sum. Using $\|\omega_{\mathbf{j}}\| = \frac{2\pi}{L} \|\mathbf{j}\|$ and treating the sum over $\mathcal{H} \setminus \{\mathbf{0}\}$ as a Riemann sum, which is approximated by an integral in spherical coordinates:

$$\begin{aligned}
 \|\tilde{c}_n\|_{L^\infty} &\leq \sum_{\mathbf{j} \in \mathcal{H}} |\tilde{\alpha}_{n;\mathbf{j}}| \\
 &\leq \sum_{\mathbf{j} \in \mathcal{H}} |\tilde{\alpha}_{0;\mathbf{j}}| + \frac{M_0}{\lambda^2} + \sum_{\mathbf{j} \in \mathcal{H} \setminus \{\mathbf{0}\}} \frac{M_0 L^2}{4\pi^2 \|\mathbf{j}\|^2} \\
 &\leq \sum_{\mathbf{j} \in \mathcal{H}} |\tilde{\alpha}_{0;\mathbf{j}}| + \frac{M_0}{\lambda^2} + \frac{M_0 L^2}{4\pi^2} \int_1^{\frac{\sqrt{3}}{2}H} \frac{1}{r^2} \cdot 4\pi r^2 dr \\
 (3.74) \quad &\leq C_{\text{stab}} H + C_0,
 \end{aligned}$$

where $C_{\text{stab}} = \frac{\sqrt{3}M_0 L^2}{2\pi}$ and $C_0 = \sum_{\mathbf{j} \in \mathcal{H}} |\tilde{\alpha}_{0;\mathbf{j}}| + \frac{M_0}{\lambda^2} - \frac{M_0 L^2}{\pi}$ are constants.

Regarding the gradient $\nabla \tilde{c}$, the SIPF- r method employs a specific discretization to handle the singularity of the Green's function $\mathcal{K}_{\epsilon, \delta t}$. According to Algorithm 2.2, the gradient at a particle position \tilde{X}_n^p is computed as:

$$\begin{aligned}
 \nabla \tilde{c}(\tilde{X}_n^p, t_n) &= -\frac{\epsilon}{\delta t} \frac{L^3}{H^3} \sum_{\mathbf{k} \in \mathcal{H}} \nabla_{\mathbf{x}} \mathcal{K}_{\epsilon, \delta t}(\tilde{X}_n^p + \bar{X}_n^p - \mathbf{x}_{\mathbf{k}}) \tilde{c}_{n-1}(\mathbf{x}_{\mathbf{k}} - \bar{X}_n^p) \\
 (3.75) \quad &\quad - \frac{M_0}{R} \sum_{s \in C_p, s \neq p} \nabla_{\mathbf{x}} \mathcal{K}_{\epsilon, \delta t}(\tilde{X}_n^p - \tilde{X}_n^s),
 \end{aligned}$$

where the spatial shift $\bar{X}_n^p = \frac{L}{2H} + \lfloor \frac{\tilde{X}_n^p}{L/H} \rfloor \frac{L}{H} - \tilde{X}_n^p$ ensures that the evaluation point is bounded away from the singularity of Green's function at grid points $\mathbf{x}_{\mathbf{k}}$. Specifically, let $r := \|\tilde{X}_n^p + \bar{X}_n^p - \mathbf{x}_{\mathbf{k}}\| \geq \frac{L}{2H}$ and $\beta = \sqrt{\lambda^2 + \epsilon/\delta t}$. The gradient of the Green's function satisfies

$$(3.76) \quad \left\| \frac{\epsilon}{\delta t} \nabla \mathcal{K}_{\epsilon, \delta t}(\tilde{X}_n^p + \bar{X}_n^p - \mathbf{x}_{\mathbf{k}}) \right\| \leq \beta^2 \frac{e^{-\beta r}}{4\pi} \left(\frac{1}{r^2} + \frac{\beta}{r} \right).$$

Letting $y = \beta r$, and using the inequality $\sup_{y \geq 0} y^k e^{-y} = (k/e)^k$, we can bound the term to be independent of β (and thus independent of δt):

$$\begin{aligned}
 \sup_{\beta > 0} \left(\frac{\beta^2}{r^2} e^{-\beta r} + \frac{\beta^3}{r} e^{-\beta r} \right) &= \frac{1}{r^4} \sup_y (y^2 e^{-y} + y^3 e^{-y}) \\
 (3.77) \quad &\leq \frac{1}{(L/2H)^4} \left(\frac{4}{e^2} + \frac{27}{e^3} \right).
 \end{aligned}$$

Since $\|\tilde{c}_{n-1}\|_{L^\infty}$ is bounded (as shown above) and the sum over $\mathbf{k} \in \mathcal{H}$ is finite for a fixed H , the term T_1 is uniformly bounded by a constant depending on H but independent of δt .

For the second term in Eq. (3.75), the RBM excludes self-interaction ($s \neq p$). For any fixed grid resolution H , the corresponding effective kernel corresponds to a spectrally truncated approximation that is smooth. Thus, for any finite number of particles, this sum is finite.

Combining these results, $\|\nabla \tilde{c}_n\|_{L^\infty(\Omega)} \leq C_{\text{reg}}(H)$ is guaranteed by the algorithm's design, where the L^∞ -norm for the vector-valued gradient is defined by $\|\nabla \tilde{c}_n\|_{L^\infty(\Omega)} := \sup_{\mathbf{x} \in \Omega} \|\nabla \tilde{c}_n(\mathbf{x})\|_{L^2}$ with $C_{\text{reg}}(H)$ is a constant depending on H , L , M_0 , and λ . \square

This lemma confirms that the boundedness condition in Assumption 2 is not merely an external hypothesis but a property guaranteed by the SIPF- r method itself. This demonstrates that the SIPF- r method effectively regularizes the singular Keller-Segel kernel. While the exact solution may exhibit finite-time blow-up (where $\|\nabla c\| \rightarrow \infty$), the numerical field remains finite for any fixed Fourier mode H . This unconditional numerical stability ensures that the algorithm is robust: it enables the simulation of blow-up phenomena by capturing the solution's growth trend as H increases, while avoiding numerical breakdown at fixed resolutions.

4. Numerical Experiments. The numerical experiments are organized into three main parts to evaluate the SIPF- r method. In Subsection 4.1, we validate the SIPF- r method by quantifying its accuracy against a high-resolution radial finite difference benchmark and verifying its convergence rates with respect to the time step and batch size. Subsection 4.2 investigates the method's capability to detect finite-time blow-up phenomena and critical mass thresholds under various conditions. Finally, Subsection 4.3 provides empirical verification of the key theoretical assumptions used in our analysis, specifically the spatial Lipschitz continuity of the concentration gradient.

4.1. Validation of the SIPF- r Method.

4.1.1. Comparison with FDM. We first demonstrate the accuracy of the SIPF- r method. In the radially symmetric case, the fully parabolic KS system (1.1) in 3D can be expressed as $\rho(x, y, z, t) = \rho(r, t)$ and $c(x, y, z, t) = c(r, t)$, where $r = \sqrt{x^2 + y^2 + z^2}$. The system is then rewritten as follows in 1D:

$$(4.1) \quad \begin{cases} \rho_t = \mu \left(\frac{\partial^2 \rho}{\partial r^2} + \frac{2}{r} \frac{\partial \rho}{\partial r} \right) - \chi \left(\frac{\partial \rho}{\partial r} \frac{\partial f}{\partial r} + \rho \cdot \left(\frac{\partial^2 f}{\partial r^2} + \frac{2}{r} \frac{\partial f}{\partial r} \right) \right), \\ \epsilon c_t = \left(\frac{\partial^2 c}{\partial r^2} + \frac{2}{r} \frac{\partial c}{\partial r} \right) - \lambda^2 c + \rho. \end{cases}$$

The radial representation in 1D allows us to compute a reference solution using a very fine mesh by the finite difference method (FDM). It will serve as a benchmark to quantify the accuracy of the SIPF- r method in 3D. We define the relative error between the cumulative distribution functions (CDFs) obtained from the FDM and the SIPF- r method as

$$(4.2) \quad \text{Relative Error} = \frac{1}{N} \sum_{i=1}^N \begin{cases} 0, & \text{if } F_{\text{FDM}}(s_i) = 0, \\ \frac{|F_{\text{SIPF-}r}(s_i) - F_{\text{FDM}}(s_i)|}{F_{\text{FDM}}(s_i)}, & \text{otherwise,} \end{cases}$$

where $F_{\text{SIPF-}r}(s_i)$ and $F_{\text{FDM}}(s_i)$ represent the CDFs of ρ computed via the SIPF- r and FDM methods respectively, and s_i denotes the i -th radial mesh point in the FDM, which are the discrete points along the radial direction starting from the origin. To ensure the relative error is well-defined, we set it to zero wherever $F_{\text{FDM}}(s_i) = 0$.

Here, the initial distribution ρ_0 is assumed to be a uniform distribution over a ball centered at $(0, 0, 0)^T$ with radius 1. The model parameters are chosen as follows:

$$(4.3) \quad \mu = \chi = 1, \quad \epsilon = 10^{-4}, \quad \lambda = 10^{-1}.$$

For the numerical computation, we use $H = 24$ Fourier basis functions in each spatial dimension to discretize the chemical concentration c and use $P = 10000$ particles to represent the approximated distribution ρ , where the batch size in Algorithm 2.2 is $R = \lfloor \sqrt{P} \rfloor = 100$. The computational domain is $\Omega = [-L/2, L/2]^3$, where $L = 8$, and the total mass is chosen to be $M_0 = 20$. The evolution of c and ρ is computed using Algorithm 2.3 with a time step size $\delta t = 10^{-4}$, up to the final simulation time $T = 0.1$.

In Fig. 1, we present the evolution of particles over time, showing the dynamic behavior of ρ . Additionally, in Fig. 2, we compare the cumulative probability curves of ρ obtained from the radial FDM and the SIPF- r method at $T = 0.1$, with a mean relative error of 0.05512 as defined in Eq. (4.2). This comparison demonstrates that the SIPF- r algorithm achieves high accuracy in approximating the true solution. These results validate the effectiveness of the SIPF- r algorithm in capturing the behavior of the particle distribution.

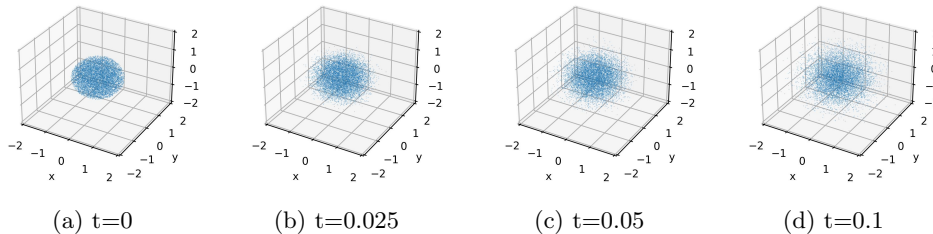


Fig. 1: Scatter plot of particles with $M_0 = 20$.

4.1.2. Convergence of the SIPF- r Method. In this subsection, we validate the convergence of the SIPF- r method numerically. Based on Eq. (3.68), the error between \tilde{c} and c can be quantified by the L^2 error between their Fourier coefficients $\tilde{\alpha}$ and α . We adopt the same initial conditions as in Subsection 4.1.1. To eliminate the uncertainty introduced by the RBM, the reference solution is computed using the original SIPF method [37] with parameters $\delta t = 10^{-6}$, $H = 24$, and $P = 10000$. Additionally, we set $M_0 = 20, T = 0.01$ to ensure that the system remains free of singularities, as verified in Fig. 3 of [37].

To investigate the convergence with respect to the time step δt , we vary δt from $2^{-8}T$ to $2^{-4}T$. Since Theorem 3.2 holds with high probability, we perform 100 independent experiments for each δt to empirically validate the algorithm’s accuracy. The mean L^2 error of the Fourier coefficients is computed over these 100 trials. As shown in Fig. 3a, the slope of the mean L^2 error versus δt on a logarithmic scale indicates an

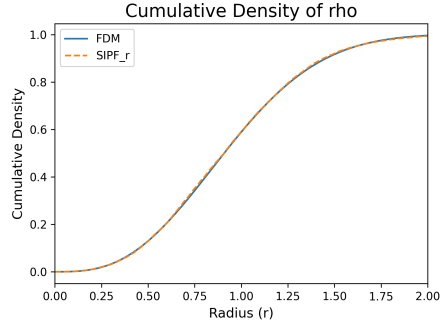


Fig. 2: Cumulative distribution of ρ computed by the SIPF- r method and radial FDM.

approximate first-order convergence rate, with $e(\delta t) = \mathcal{O}(\delta t^{1.023})$. This result aligns with the theoretical bound given in Eq. (3.8) of Theorem 3.2.

Furthermore, we examine the mean L^2 error of $\tilde{c}(\cdot, T)$ for varying batch sizes $R = 100, 200, 400, 800, 1600$, while keeping $P = 10000$. From Eq. (3.8), with other parameters fixed, the theoretical L^2 error of \tilde{c} with respect to the batch size R should scale as $\mathcal{O}(R^{-\frac{1}{2}})$. This is empirically verified in Fig. 3b, where the fitted convergence rate is $e(R) = \mathcal{O}(R^{-0.495})$, closely matching the theoretical prediction.

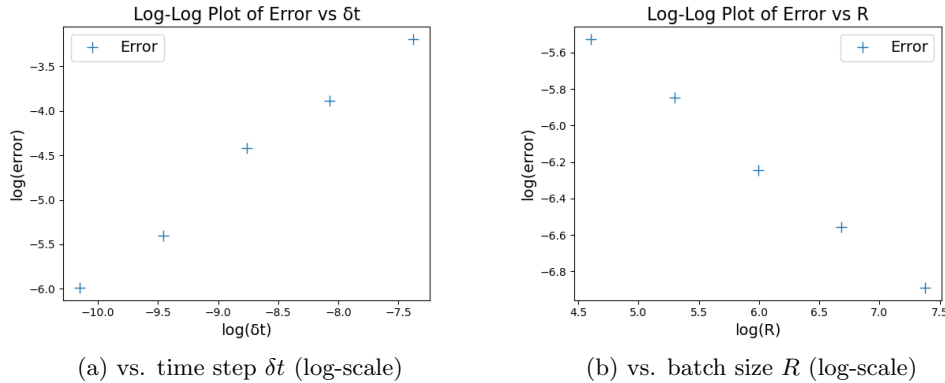


Fig. 3: L^2 error of \tilde{c} in the SIPF- r method.

4.2. Numerical Detection of Finite-time Blow-up. While the error analysis in Section 3 assumes regular solutions, our algorithm can effectively detect finite-time blow-up phenomena under practical conditions. The parameters are the same as in Eq. (4.3), with the radial system (4.1) serving as a reference benchmark. We consider a more concentrated initial condition than in the preceding subsections: a uniform distribution within a ball of radius $r = 1.5$.

Fig. 4 illustrates the effect of varying the initial mass M_0 on solution behavior at $T = 2$. Figs. 4a and 4b show particle distributions for $M_0 = 72$ and $M_0 = 73$, respectively, with the latter exhibiting clear focusing and potential blow-up. In Fig. 4c,

we present the maximum value of c over space at $T = 2$ for different initial masses, computed via the radial FDM as a benchmark. We denote

$$(4.4) \quad \|c\|_{\infty, \text{FDM}} = \sup_r |c(r, T)|.$$

The FDM exhibits numerical instabilities (marked in red) for initial masses between 72 and 73, which matches the blow-up transition observed in our particle method in Fig. 4b. Remarkably, the focusing and potential blow-up are captured with only $P = 10^4$ particles and moderate H , demonstrating the algorithm’s ability to detect singularities without stringent theoretical assumptions.

To further investigate blow-up detection with our method, we examine the maximum chemical concentration c as a function of time T for different discretization levels H and masses M_0 . As shown in Fig. 5, when $M_0 = 40$ (Fig. 5a), the maximum c remains stable and shows minimal variation across H values, indicating a non-blow-up regime. In contrast, for $M_0 = 100$ (Fig. 5b), the maximum c exhibits strong dependence on H , with curves diverging significantly. Notably, this blow-up signature is visible even with coarse discretization ($H = 8$ vs $H = 12$), demonstrating that singularity detection does not require high-resolution computations. The divergence of solutions at different H levels provides a practical diagnostic for intense focusing and blow-up phenomena without demanding highly refined discretizations.

We then demonstrate that our method can also capture focusing and potential blow-up for non-radial initial data. We consider two non-overlapping spheres of radius $r = 0.5$ with centers at $(0.6, 0, 0)$ and $(-0.6, 0, 0)$, each containing equal mass $M_0/2$ (total mass $M_0 = 100$). Fig. 6 shows the time evolution for two different mass regimes: the top row ($M_0 = 10$) remains stable at all times, while the bottom row ($M_0 = 100$) exhibits clear focusing towards blow-up formation at $T = 0.2$. This demonstrates that our algorithm effectively detects blow-up even for non-symmetric initial configurations, highlighting its robustness beyond the radially symmetric case.

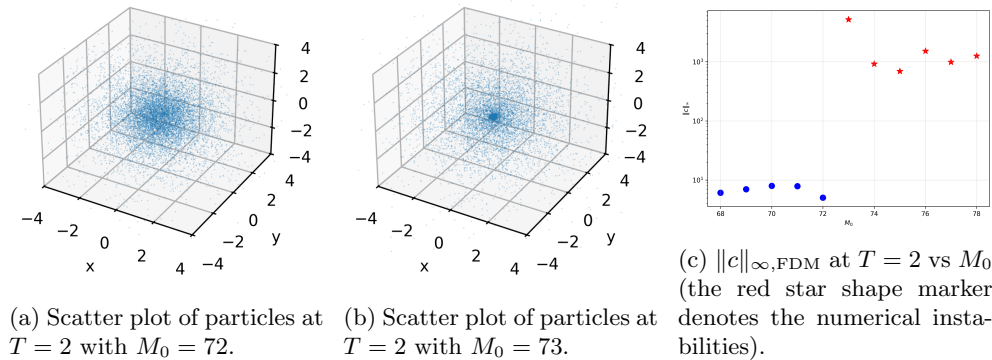


Fig. 4: Effects of initial mass M_0 on focusing behavior (finite time blowup).

4.3. Validation of Theoretical Assumptions. To verify the spatial Lipschitz continuity in Assumption 2(a), we adjust the spatial discretization by varying H from 6 to 24. At the final time $T = 0.1$, we randomly select 1000 pairs of particle points from a total of 10,000 particles in each calculation. The spatial Lipschitz constant

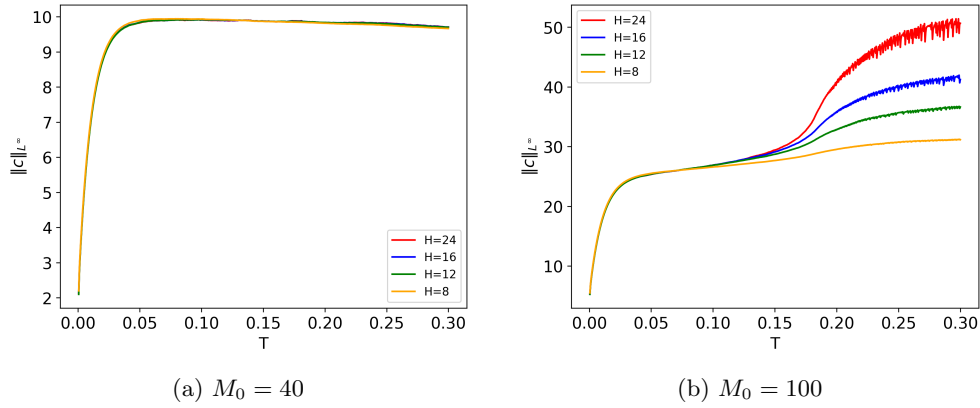


Fig. 5: Maximum chemical concentration c vs computation time T for different discretization parameters H and total masses M_0

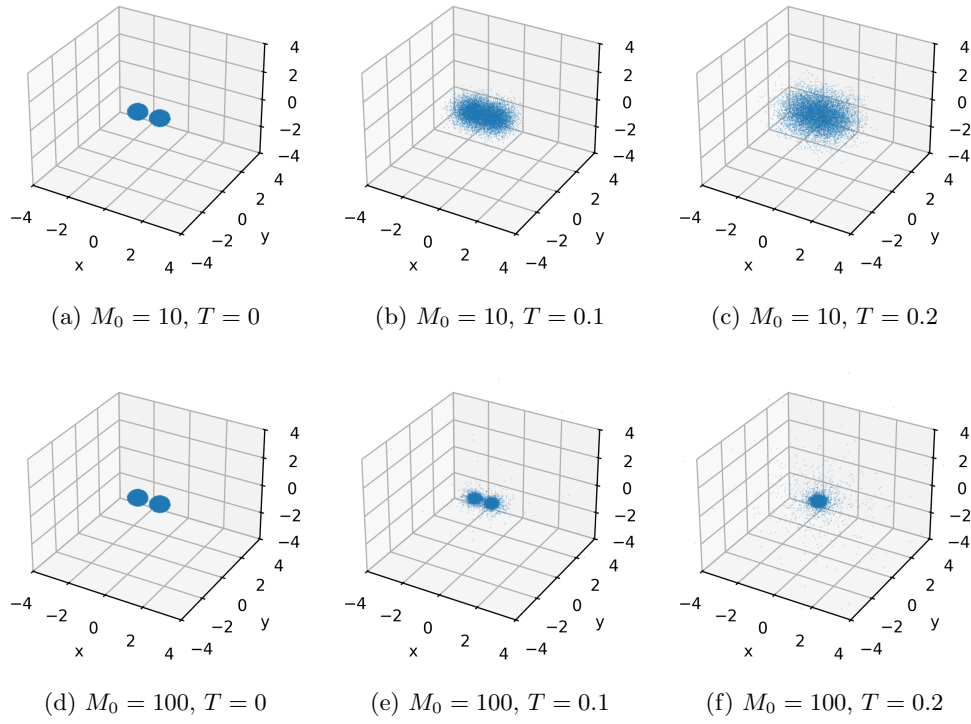


Fig. 6: Finite-time blow-up detection for non-radial initial data (two spheres). Top row: $M_0 = 10$, stable evolution at times $T = 0, 0.1, 0.2$. Bottom row: $M_0 = 100$, evolution showing blow-up formation at $T = 0.2$. Both simulations use $P = 10^4$ particles, $H = 24$, and initial spheres of radius $r = 0.5$ centered at $(\pm 0.6, 0, 0)$.

$L(H)$ for $\nabla\tilde{c}$ is defined as the maximum ratio of the gradient difference to the spatial distance over all pairs of particle points $\{\mathbf{x}, \mathbf{y}\}$:

$$(4.5) \quad L(H) := \max_{\{\mathbf{x}, \mathbf{y}\}} \frac{\|\nabla\tilde{c}(\mathbf{x}, T) - \nabla\tilde{c}(\mathbf{y}, T)\|}{\|\mathbf{x} - \mathbf{y}\|}.$$

The results, shown in Table 1, list the computed Lipschitz constant $L(H)$ for each value of H . The variation in these values is relatively small, confirming that the spatial Lipschitz continuity holds for $\nabla\tilde{c}$ computed by the SIPF- r method.

Fourier modes (H)	Spatial Lipschitz constant ($L(H)$)
6	0.002085
12	0.002106
18	0.002036
24	0.001957

Table 1: Spatial Lipschitz constant of $\nabla\tilde{c}$ vs. H .

5. Conclusions. In this paper, we introduced a random batch variant [17] of the original SIPF method [37] to compute the 3D fully parabolic KS systems. This modification leverages the randomness in batch sampling to bypass the mean-field limit, reducing computational complexity without sacrificing accuracy. We developed a comprehensive convergence analysis for the fully coupled particle-field system. Specifically, we proved the convergence with high probability for both the density $\tilde{\rho}(\mathbf{x}, t)$ and the concentration field $\tilde{c}(\mathbf{x}, t)$ to their respective exact solutions $\rho(\mathbf{x}, t)$ and $c(\mathbf{x}, t)$. The error bounds reveal a dependence on δt , H , and P , with the density and concentration field exhibiting distinct but interrelated convergence behaviors.

Numerical experiments validated these theoretical rates and demonstrated the robustness of the SIPF- r method. Notably, the algorithm effectively captures focusing and potential finite-time blow-up phenomena subject to critical mass thresholds in three space dimensions even under discretization parameters less restrictive than those required by the worst-case scenario theoretical bounds. Future work will focus on refining the error estimates, particularly alleviating the potential overestimation of the dependence on the Fourier mode H , and improving the algorithm’s efficiency in high-dimensional settings. Extending the SIPF- r method to systems with anisotropic interactions or more complex chemo-attractant dynamics also presents a promising direction for further research.

Acknowledgements. ZW was partially supported by NTU SUG-023162-00001 and MOE AcRF Tier 1 Grant RG17/24. JX was partially supported by NSF grant DMS-2309520, the Swedish Research Council grant no. 2021-06594 at the Institut Mittag-Leffler in Djursholm, Sweden, and the E. Schrödinger Institute in Vienna, Austria, during his stay in the Fall of 2025. ZZ was partially supported by the National Natural Science Foundation of China (Projects 12171406 and 92470103), the Hong Kong RGC grant (projects 17304324 and 17300325), the Seed Funding Programme for Basic Research (HKU), and the Hong Kong RGC Research Fellow Scheme 2025. The simulations were performed on the research computing facilities of the Information Technology Services at the University of Hong Kong.

- [1] N. BELLOMO, A. BELLOUQUID, Y. TAO, AND M. WINKLER, *Toward a mathematical theory of Keller-Segel models of pattern formation in biological tissues*, *Mathematical Models and Methods in Applied Sciences*, 25 (2015), pp. 1663–1763.
- [2] F. BUBBA, C. POUCHOL, N. FERRAND, G. VIDAL, L. ALMEIDA, B. PERTHAME, AND M. SABBAH, *A chemotaxis-based explanation of spheroid formation in 3D cultures of breast cancer cells*, *Journal of Theoretical Biology*, 479 (2019), pp. 73–80.
- [3] Z. CAI, J.-G. LIU, AND Y. WANG, *Convergence of random batch method with replacement for interacting particle systems*, arXiv preprint arXiv:2407.19315, (2024).
- [4] A. CHERTOCK, Y. EPSHTEYN, H. HU, AND A. KURGANOV, *High-order positivity-preserving hybrid finite-volume-finite-difference methods for chemotaxis systems*, *Advances in Computational Mathematics*, 44 (2018), pp. 327–350.
- [5] A. CHERTOCK AND A. KURGANOV, *A second-order positivity preserving central-upwind scheme for chemotaxis and haptotaxis models*, *Numerische Mathematik*, 111 (2008), pp. 169–205.
- [6] K. CRAIG AND A. BERTOZZI, *A blob method for the aggregation equation*, *Mathematics of Computation*, 85 (2016), pp. 1681–1717.
- [7] Y. EPSHTEYN, *Upwind-difference potentials method for Patlak-Keller-Segel chemotaxis model*, *Journal of Scientific Computing*, 53 (2012), pp. 689–713.
- [8] Y. EPSHTEYN AND A. IZMIRLIOGLU, *Fully discrete analysis of a discontinuous finite element method for the Keller-Segel chemotaxis model*, *Journal of Scientific Computing*, 40 (2009), pp. 211–256.
- [9] I. FATKULLIN, *A study of blow-ups in the Keller-Segel model of chemotaxis*, *Nonlinearity*, 26 (2012), p. 81.
- [10] F. FILBET, *A finite volume scheme for the Patlak-Keller-Segel chemotaxis model*, *Numerische Mathematik*, 104 (2006), pp. 457–488.
- [11] D. GODINHO AND C. QUININAO, *Propagation of chaos for a subcritical Keller-Segel model*, in *Annales de l’IHP Probabilités et Statistiques*, vol. 51, 2015, pp. 965–992.
- [12] I. GOODFELLOW, Y. BENGIO, AND A. COURVILLE, *Deep learning*, MIT press, 2016.
- [13] J. HAŠKOVEC AND C. SCHMEISER, *Stochastic particle approximation for measure valued solutions of the 2d Keller-Segel system*, *Journal of Statistical Physics*, 135 (2009), pp. 133–151.
- [14] M. A. HERRERO, E. MEDINA, AND J. J. VELÁZQUEZ, *Self-similar blow-up for a reaction-diffusion system*, *Journal of Computational and Applied Mathematics*, 97 (1998), pp. 99–119.
- [15] Z. HUANG, S. JIN, AND L. LI, *Mean field error estimate of the random batch method for large interacting particle system*, *ESAIM: Mathematical Modelling and Numerical Analysis*, 59 (2025), pp. 265–289.
- [16] S. JIN AND L. LI, *Random batch methods for classical and quantum interacting particle systems and statistical samplings*, in *Active Particles, Volume 3: Advances in Theory, Models, and Applications*, Springer, 2021, pp. 153–200.
- [17] S. JIN, L. LI, AND J.-G. LIU, *Random batch methods (RBM) for interacting particle systems*, *Journal of Computational Physics*, 400 (2020), p. 108877.
- [18] E. F. KELLER AND L. A. SEGEL, *Initiation of slime mold aggregation viewed as an instability*, *Journal of Theoretical Biology*, 26 (1970), pp. 399–415.
- [19] T. W. KÖRNER, *Fourier Analysis*, Cambridge University Press, 2022.
- [20] X. H. LI, C.-W. SHU, AND Y. YANG, *Local discontinuous Galerkin method for the Keller-Segel chemotaxis model*, *Journal of Scientific Computing*, 73 (2017), pp. 943–967.
- [21] J.-G. LIU, L. WANG, AND Z. ZHOU, *Positivity-preserving and asymptotic preserving method for 2d Keller-Segel equations*, *Mathematics of Computation*, 87 (2018), pp. 1165–1189.
- [22] J.-G. LIU AND R. YANG, *A random particle blob method for the Keller-Segel equation and convergence analysis*, *Mathematics of Computation*, 86 (2017), pp. 725–745.
- [23] J.-G. LIU AND R. YANG, *Propagation of chaos for the Keller-Segel equation with a logarithmic cut-off*, *Methods and Applications of Analysis*, 26 (2019), pp. 319–348.
- [24] A. I. MARKUSHEVICH, *Theory of functions of a complex variable*, American Mathematical Society, 2013.
- [25] T. NAGAI, *Blow-up of radially symmetric solutions to a chemotaxis system*, *Advances in Mathematical Sciences and Applications*, 5 (1995), p. 581.
- [26] K. J. PAINTER, *Mathematical models for chemotaxis and their applications in self-organisation phenomena*, *Journal of Theoretical Biology*, 481 (2019), pp. 162–182.
- [27] C. S. PATLAK, *Random walk with persistence and external bias*, *The Bulletin of Mathematical Biophysics*, 15 (1953), pp. 311–338.
- [28] B. PERTHAME, *Transport equations in biology*, Springer Science & Business Media, 2006.
- [29] N. SAITO, *Conservative upwind finite-element method for a simplified Keller-Segel system modelling chemotaxis*, *IMA Journal of Numerical Analysis*, 27 (2007), pp. 332–365.

- [30] N. SAITO, *Error analysis of a conservative finite-element approximation for the Keller-Segel system of chemotaxis*, Communications on Pure and applied Analysis, 11 (2011), pp. 339–364.
- [31] N. SAITO AND T. SUZUKI, *Notes on finite difference schemes to a parabolic-elliptic system modelling chemotaxis*, Applied Mathematics and Computation, 171 (2005), pp. 72–90.
- [32] J. A. SHERRATT, *Chemotaxis and chemokinesis in eukaryotic cells: The Keller-Segel equations as an approximation to a detailed model*, Bulletin of Mathematical Biology, 56 (1994), pp. 129–146.
- [33] M. SOMMERFELD, J. SCHRIEBER, Y. ZEMEL, AND A. MUNK, *Optimal transport: Fast probabilistic approximation with exact solvers*, Journal of Machine Learning Research, 20 (2019), pp. 1–23.
- [34] A. STEVENS, *The derivation of chemotaxis equations as limit dynamics of moderately interacting stochastic many-particle systems*, SIAM Journal on Applied Mathematics, 61 (2000), pp. 183–212.
- [35] Z. WANG, J. XIN, AND Z. ZHANG, *DeepParticle: learning invariant measure by a deep neural network minimizing Wasserstein distance on data generated by an interacting particle method*, Journal of Computational Physics, 464 (2022), p. 111309.
- [36] Z. WANG, J. XIN, AND Z. ZHANG, *A DeepParticle method for learning and generating aggregation patterns in multi-dimensional Keller-Segel chemotaxis systems*, Physica D: Nonlinear Phenomena, 460 (2024), p. 134082.
- [37] Z. WANG, J. XIN, AND Z. ZHANG, *A novel stochastic interacting particle-field algorithm for 3d parabolic-parabolic Keller-Segel chemotaxis system*, Journal of Scientific Computing, 102 (2025), pp. 1–23.
- [38] G. ZHOU AND N. SAITO, *Finite volume methods for a Keller-Segel system: discrete energy, error estimates and numerical blow-up analysis*, Numerische Mathematik, 135 (2017), pp. 265–311.